Florian Koller

Stellar reflection nebulae

Bachelor Thesis

University of Graz

Institute of Physics /
Geophysics, Astrophysics und Meteorology (IGAM)

Supervisor: Dr. Thorsten Ratzka

Graz, September 2016

Contents

1 Abstract

This Bachelor Thesis has the goal to detect, image, describe, and analyze reflection nebulae of pre-main sequence stars and protoplanetary nebulae.
To achieve this, the 50 cm Cassegrain telescope at the location Observatorium Lustbühel Graz (OLG) was used. The telescope is operated by the Institute of Geophysics, Astrophysics and Meteorology (IGAM).
Additionally, this work deals with the question what is technically possible with this telescope at this location. The best possible result to analyze the nebulae is sought with the help of data reduction and adapted data processing.
Pixel size, spatial resolution and seeing were determined. 17 pre-main sequence stars and 2 protoplanetary nebulae were observed, with focus on bright and extended nebulae with much visible structure or highly variable nebulae like NGC 2261 (Hubble's Variable Nebula), NGC 1555 (Hind's Variable Nebula) or PV Cephei. Optimal observation conditions for young stellar objects and reasonable pixel resolution were discussed.

2 Kurzbeschreibung

Diese Bachelorarbeit verfolgt das Ziel Reflektionsnebel um Vor-Hauptreihensterne, sowie Protoplanetarische Reflektionsnebel zu detektieren, abzubilden, zu beschreiben und physikalisch auszuwerten.
Zur Verfügung stand dafür das vom Institutsbereich für Geophysik, Astrophysik und Meteorologie (IGAM) des Instituts für Physik der Karl-Franzens Universität betriebene 50cm-Cassegrain-Spiegelteleskop am Standort Observatorium Lustbühel Graz (OLG).
Diese Arbeit geht zusätzlich darauf ein, was technisch mit diesem Teleskop an diesem Standort möglich ist. Zudem wird durch Datenreduktion und Nachbearbeitung das bestmögliche Ergebnis aus den aufgenommenen Datensätzen zur Beschreibung der Nebel angestrebt.
Bestimmt wurden die Pixelgröße der Aufnahmen, das Auflösungsvermögen sowie das Seeing. Es wurden 17 Vor-Hauptreihensterne und 2 Protoplanetarische Nebel beobachtet. Ein Fokus wurde auf helle und weit ausgedehnte Nebel mit viel Struktur oder stark veränderliche Nebel gelegt, beispielsweise NGC 2261 (Hubble's Variabler Nebel), NGC 1555 (Hind's Variabler Nebel) oder PV Cephei. Die optimalen Bedingungen zum Beobachten von Vor-Hauptreihensterne und sinnvolle Pixelauflösung wurden diskutiert.

3 Basis

This section gives a brief summary on reflection nebulae and stellar evolution in general. Additionally, information about the technical aspects of the observations is provided.

3.1 Theory

A reflection nebula is interstellar matter (ISM) that is illuminated by a nearby star and reflects/scatteres the star's light. This ISM consists of gas (atoms, molecules, ions) and dust (solid particles). While the gas makes up most of the mass of the interstellar matter, it is the dust that is responsible for reflection nebulae. The gas of the ISM gets visible when being ionized by the photons of a nearby star. Is the photon energy insufficient, however, the light only gets scattered by the dust particles in the ISM, making the ISM visible. The frequency of the scattered light of the reflection nebula is similar to the light of the illuminating star. This fact also led to the discovery of reflection nebulae (and to the discrimination from emission nebulae).

3.1.1 Interstellar dust and Scattering

The interstellar dust consists mainly of silicates and carbonous particles formed by winds and expandings shells of evolved stars. In circumstellar disks, the dust particles can grow to larger particles or crystalline structures. The main part of the silicate dust is poryxene and olivene, both initially amorphous.
The size range is given with 0.005 - 1 μm for graphite particles and 0.025 - 0.25 μm for other materials with the size distribution following a power law $a^{-3.5}$ ([1]Mathis et al. 1977). The term reflection is somewhat misleading, as the light gets mainly scattered (reflection may occur at larger particles).
There are three scattering processes important for interstellar dust, depending on the factor α:

$$\alpha = \frac{\pi \cdot D}{\lambda} \tag{1}$$

Where $\pi \cdot D$ stands for the size of the particle and λ for the wavelength of the radiation. The tree different cases are:

- $\alpha \gg 1$, shadowing, occurs when the particle is much larger than the photon's wavelength
- $\alpha \approx 1$, when the size of the particle and the wavelength are similar,; results in a scattering proportional to λ^{-1}; Mie-scattering
- $\alpha \ll 1$, when the particle is much smaller than the wavelength; results in a scattering proportional to λ^{-4}; Rayleigh-scattering.

From these scattering types we can conclude that bluer wavelengths get more scattered, and thus reflection nebulae usually appear bluer.

The scattering is also the cause of an effect called extinction: stars appear redder when more interstellar dust is in the line-of-sight as the shorter wavelengths get scattered away. The dust itself re-emits the energy in the infrared, which is a important cooling factor of the ISM and crucial for star formation. Polarization of light is also possible due to elongated grains aligned in the magnetic fields of the ISM. Since no polarization filter was used for the observations, this topic will not be further discussed.

3.1.2 Stellar evolution - young stellar objects YSOs

Giant molecular clouds (consisting of ISM) are the starting points in the stellar evolution. The gravitational collapse of the ISM breaks the cloud into smaller fragments. In these fragments, further collapsing of gas leads to an increase of pressure and temperature. The gravitational pressure presses against the thermal pressure. The first stop of the gravitational collapse is reached at densities of about $2 \cdot 10^{-10} gm^{-3}$. A first stable hydrostatic core with 0.01 $M_\odot$ is formed while matter from the surrounding material still falls onto the protostar. If the temperature of 2000K is reached, a second collapse starts as the hydrogen molecules dissociate. A second core with 0.001 $M_\odot$ is formed and the collapse is halted, while matter continues to fall onto the protostar.
Young stellar objects are classified in 4 different classes (Class 0, I, II and III). The first two classes are called the protostellar phase, beginning with the just described process of forming a hydrostatic core. They radiate mainly in the far-infrared and submillimeter range of the spectrum. The lifespan of these classes are relatively short, ranging from $> 3 \cdot 10^4 a$ (Class 0) up to $1 \cdot 10^7 a$ (Class III). The classification is done by using the spectral energy distribution (SED) and determining its slope at infrared wavelengths, which will not be further discussed here. The Class I protostars reside within an envelope of circumstellar material. A disk around the star forms due to the rotation of the system (conservation of angular momentum) and the stellar wind blows away the material perpendicular to the disk.
Eventually, the star becomes optically visible, reaching the birthline in the Hertzsprung-Russel diagram (HRD) as a pre-main sequence star (PMS, which ranges from Class II to III). A Class II star is called a classical T Tauri star (CTTS). The star has now aquired most of its mass, but no nuclear fusion has started yet. Accretion is happening in the circumstellar disk. The PMS Class III star is called weak-line T Tauri star (WTTS). It shows weak or no emmission lines, the accretion in the disk is completed and the disk is dispersed. Still, the main sequence of the HRD is not reached. The source of energy for pre-main sequence stars are gravitational contractions, making these stars highly variable. PMS stars are located above the main sequence in the HRD. They have larger radii than main sequence stars and are fully convective as long as they are on the Hayashi track (vertical in the HRD; luminosity as well as radius decreases). If the PMS is massive enough, it follows the Henyey track (almost horizontal in the HRD; temperature increases). The tracks depend on the mass and the chemical composition of the star. The star becomes a main sequence star once the core temperature is high enough and the burning of hydrogen starts.

Two types of pre-main sequence stars are observed: T Tauri type stars (named after their prototype) and Herbig Ae/Be stars. T Tauri stars have low masses (< 2 $M_\odot$) and are very active and variable. Their spectral type is F, G, K or M. Brightness variability could be caused by inhomogenities in the surrounding disk and the high activity in general.
Herbig Ae/Be stars have higher masses (2 - 8 $M_\odot$) and are of spectral type A or B (the e in the name indicates Balmer emission lines). An infrared excess can be found in their spectra due to dust from the circumstellar disk. Like T Tauri stars they are highly variable in brightness, which could be caused their activity or inhomogenities. Both Herbig Ae/Be and T Tauri stars are recognised to be photometric variable and often have reflection nebulae nearby, which links them to a star-forming region. There are no PMS stars with higher masses than $8M_\odot$ observed in the visual or the infrared as these stars evolve too quickly and are deeply embedded in their envelopes.
Another classification of a PMS star is the FU Orionis type star, which is a star that undergoes extreme changes in magnitude and spectral type. They are believed to be T Tauri stars with an episodic high mass transfer from their accretion disk.
UX Orionis type stars are also variable PMS stars which show deep minima in their brightness. Their variability is probably caused by variable extinction in their circumstellar disk.

3.1.3 Herbig Haro objects

The brief description here follows [2]Schwartz 1983.

Many YSOs show Herbig Haro objects (HH) nearby. These are patches of nebulosity caused by jets from newly born stars. The jets are usually highly collimated and lie perpendicular to the accretion disk, as do the HH themselves. The outflow is in general bipolar, with two jets moving the opposite direction away from the star at high velocities. The jets collide with the ISM at supersonic speed and thus produce visible light. HHs show unusual strong emission lines in their spectra, while they are invisible at infrared wavelengths.

3.1.4 Stellar evolution- Post AGB stars

As two protoplanetary nebula caused by post-AGB stars are also observed within this thesis, a brief summary on the late evolution of a medium mass star is given here too. The description here follows the lecture 'Stellar Structure & Stellar Evolution' from lecturer Dr. Thorsten Ratzka, [3]Iben and Renzini 1983 and [4]Volk et al. 1989.

After burning the hydrogen in the core, the star leaves the main sequence. It gets cooler in the process while the hydrogen burning goes on in the shell above the core. The star expands and gets more luminous (Red Giant Branch RGB) while the core contracts and increases its temperature. A helium flash occurs, starting the helium burning in the core. The star is losing some mass in the process. The star reaches the Asymptotic Giant Branch (AGB) after running out of helium in the core and a helium burning shell forms. It again expands and gets more luminous. Later, the thermally pulsing phase where the stars repeatedly expands and then contracts is starting. It is caused by the two burning shells: with the expanding He shell, the outer H shell stops the burning process due to lesser density and cooler outer temperature of the then expanded star. When the He burning stops, the H shell contracts, re-ignites and provides He as fuel for the inner He shell. The He shell re-ignites and the process repeats. In this phase, a lot of mass is lost due to stellar winds building circumstellar envelopes. The effective temperature of the star rises, moving it to the left side of the HRD. The protoplanetary phase starts, the ejected material gets illuminated but not ionized as it is the case for later planetary nebulae. The material is moving fast outwards, forming often a bipolar structure. It is a short phase. The nebula becomes a planetary nebula (an emission nebula) as soon as the star reaches high enough temperatures to ionize the surrounding material. The star will end as a white dwarf.

3.2 Technical basis

Information on the technical aspects of the observations. Background information on the telescope, the camera, the filter is given as well as details on the Signal-to-noise ratio and the display of the images.

3.2.1 Telescope

At the Lustbühel Observatory (OLG) a 50 cm reflecting telescope of the design type Cassegrain is used. This type of telescope consists of a primary concave and a secondary convex mirror. This way, the telescope could be build mechanically short while achieving a long focal length.
The following table 1 lists the specifications of this telescope.

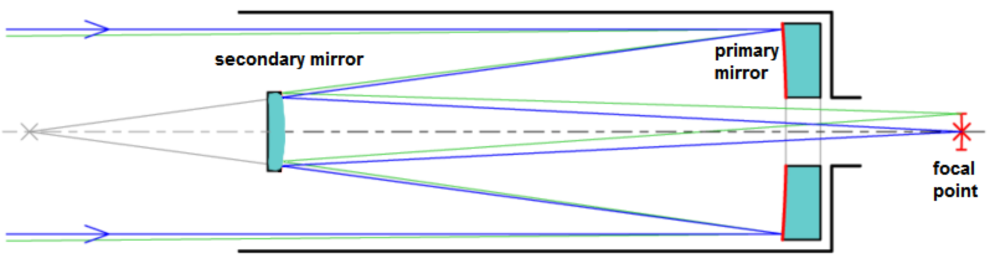

Figure 1: Scheme of a Cassegrain reflecting telescope (Source: commons.wikimedia.org)

3.2.2 Camera

The used camera is called STF-8300M (monochrome) and is manufactured by the company SBIG. Its CCD array has 3326 x 2504 pixels, resulting in approximately 8.3 megapixel. It has a optional binning mode integrated. 2x2 and 3x3 binning is possible. Binning is a procedure to read out several pixels as one, e.g. 2x2 binning groups 4

type	Cassegrain
aperture	500 mm
optical diameter primary mirror	500 mm
optical diameter secondary mirror	175 mm
focal length	4500 mm
back focus	410 mm
f-ratio	f9
field of view	61 arc min

Table 1: Specifications of the telescope

pixels to one new pixel. This improves the signal to noise ratio (SNR), but results in a lower resolution of the image.
The camera is operated with a filter wheel to get observations at different wavelengths (see 3.2.3). The camera has an integrated Peltier cooling device to achieve a low dark current. Dark current refers to thermally generated electrons that contribute to the signal. All observations were made with a cooling temperature between -10°C and -20°C.
In the resulting image, the electrons are converted to a certain number per pixel (called Analog-to-digital unit ADU, number count or count value). The conversion is given by a value called the A/D gain (0.37 $\frac{e^-}{ADU}$ for the STF-8300M). The wavelength-dependent quantum efficiency (QE, meaning incident photon to generated electron ratio) of the camera is especially important for the observations. As we can see in Fig. 2, the QE peaks at 550nm.
Another factor of the camera is the linearity (refering to the counts at longer exposure times). For expample, double exposure time should lead to a signal that is two times higher. This is not given at high count values (maximum number count for a pixel is 65536, resulting from 16 bit). The response is within about 1 % of an linear regime up to a count number of 50000 at 2x2 binning. As sometimes the structure of a nebula becomes visible at long exposure times,when some parts of the nebula would already cause high count rates, these non-linear errors can only be prevented by image stacking.

3.2.3 Filter

For the observations, a set of standard photometric filters was used. Images were taken with the passbands B, V (Johnson-Cousins-Bessell system), r and i (Sloan system). Only specific wavelengths of light pass trough these filters. B stands for blue, V for visual (which has its peak in the green part of the visual spektrum). The small r stands for red und i for (near) infrared. The dependence of the transmittance as function of the wavelength is plotted in 3 and 4. Table 2 lists wavelength informations on the filters (Source: [6]Bessel 2005).

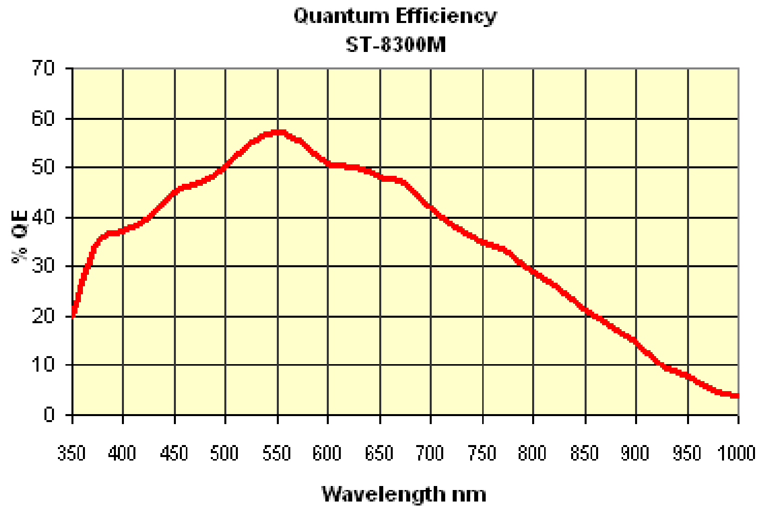

Figure 2: Quantum efficiency of the camera as function of the wavelength (Source: [5])

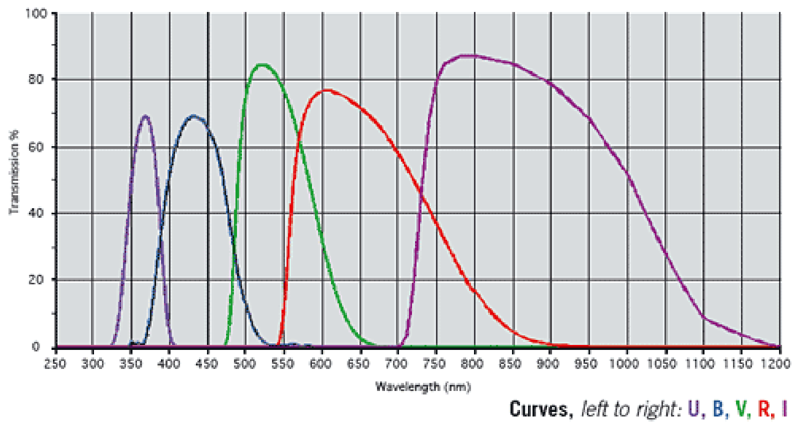

Figure 3: Johnson-Cousins-Bessell system filters (source: [7])

3.2.4 Signal-to-noise ratio and image display

The signal-to-noise ratio (SNR) is a value to determine how well a object is measured. The signal S is the number of photons we detect from a source (or in our case photons converted to electrons, according to the quantum efficiency of the camera). S is calculated by the number of electrons of the object per second times the exposure time t.

The noise N is the error in the measured flux in units of photons or electrons. There are several noise sources:

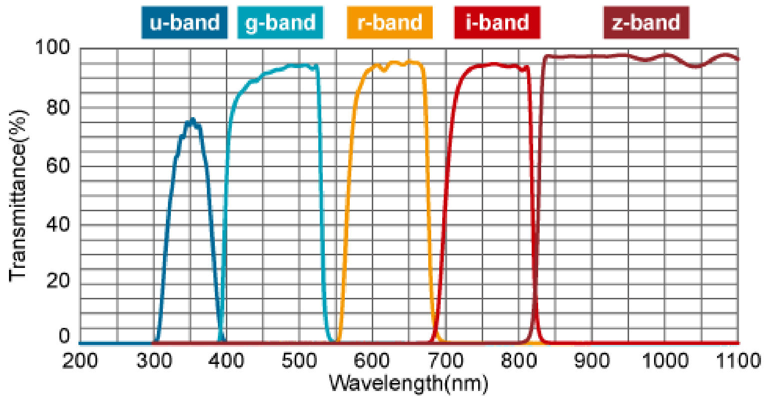

Figure 4: Sloan system filters (source: [7])

Filter Letter	λ_{eff}	$\Delta\lambda$
B	4361	890
V	5448	840
r	6122	1150
i	7439	1230

Table 2: Filter wavelength information. λ_{eff} refers to the effective wavelength midpoint in Å, $\Delta\lambda$ refers to the full width at half maximum (bandwidth) in Å

- Object noise, given by the square root of the object's signal.
- Sky noise, which is the noise from the background. It also depends on the square root of the sky's signal (in electrons per pixel per second), the object's area in pixel and the exposure time.
- Dark noise, which is caused by thermally generated electrons. Its calculation is the same as for the sky noise, with the dark current instead of the sky's signal.
- Read-out noise, generated by the amplifier while reading the detector. It does not depend on the exposure time t, and is calculated by the read out noise per pixel times the square root of the pixel area.

All these noise sources are added. The full equation for the SNR gives us:

$$\frac{S}{N} = \frac{s * t}{\sqrt{(s * t) + (n_{pix} * s_{sky} * t) + (n_{pix} * s\_dark * t) + (n_{pix} * RON^2)}} \tag{2}$$

With t being the exposure time, s the object's number of electrons per second, s_{sky} the number of electrons per second of the background per pixel, s_{dark} the number of electrons per second of the dark current per pixel, n_{pix} the surface area in pixels and RON the read out noise per pixel.

The higher the SNR is, the better. As we can see, the signal increases linearly with the exposure time, while the noise increases by a square root function of the exposure time. The dependence on the square root is a result of $\sqrt{n}$ being the standard deviation of a poisson distribution with large values n. An image with an x times longer exposure time has a $\sqrt{x}$ better SNR. To avoid the non-linear regime of the CCD and to avoid saturation of objects on the image, one can perform stacking, i.e. several images of the same objects with shorter exposure times are added. This also increases the overall signal of the object. If two images with the same exposure times are added, the SNR increases by a factor of $\sqrt{2}$. Another important point is that n_{pix} for a point source depends on the square of the seeing, meaning a low seeing is necessary for a high SNR.

The SNR can be calculated using ADUs or electrons, as it is equivalent for the calculation.
The image is mathematically a m x n matrix with every matrix value being a pixel with a certain count value. The values m and n give the pixel resolution of the image. The program SAOimage ds9 was used to display the images, to determine the count values and to perform further analyses (e.g. contour plots for nebulae). To achieve the best visibility for the nebulae, the contrast and the bias of the images are adjusted, with sometimes using an inverted image for a better contrast. As sometimes the signal from the nebula is weak in relation to the background and or the surrounding stars, the cut-off limits are adjusted as a part of changing the scale parameters. The lower cut-off limit determines which count values are displayed as black, i.e. all pixels up to this value are displayed black. The upper limit determines which count values are displayed as white, i.e. all pixels with higher values. This emphasizes the structure that lies between the limits. To further enhance structures, it is possible to use a scaling following other functions than the usual linear slope. Sometimes a logarithmic scale is more useful to show the overall image when a star is too bright and overshines the surrounding nebula.

4 Measurement and optical calculations

All data on right ascencion (R.A.) and declination (Dec.) are given in ICRS ep=J2000 and were extracted from SIMBAD [8]. There is a wide variety of designations for the observed objects; only names that are common in scientific papers are used. The V* as part of the designation indicates a variable star. As most of the observed stars are variable in nature, this indicator is not used in the following analysis.

4.1 Observation on 17 March 2016

The list of objects observed on 17 March 2016 is given in Table 3. The Moon was waxing (about 75% illuminated) and its position was in the constellation Gemini. This is a suboptimal condition as observations were made in the neighbouring constellations Orion, Taurus, Monocerus and Auriga. Many objects were just slightly above the horizon (>20° altitude) which results in bad seeing conditions. The tracking of the telescope was a little bit off, resulting in line-shaped stars after long exposure times (>120s). The light of the city of Graz (light pollution) also deteriorates the conditions. The observation time was between 7:00 p.m. and 0:00 a.m. (UTC+1).

Object	Alternative name	Time	R.A.	Dec.
V* T Tau	NGC 1555, Hind's Nebula	19:40 - 21:00	04 21 59.43	+19 32 06.4
V* AB Aur		21:20 - 21:40	04 55 45.85	+30 33 04.3
Holoea	IRAS 05327+3404	21:45 - 21:57	05 36 05.97	+34 06 12.0
V* FU Ori	CED 59	22:00 - 22:20	05 45 22.36	+09 04 12.4
V* R Mon	NGC 2261, Hubble's Variable Nebula	22:25 - 22:59	06 39 09.95	+08 44 09.1
Frosty Leo	IRAS 09371+1212	23:18 - 23:28	09 39 53.96	+11 58 52.6

Table 3: Objects observed on March, 17 2016

4.2 Observation on 14 April 2016

The list of objects observed on 14 April 2016 is given in Table 4. The Moon was waxing (about 60% illuminated) and its position was in the constellation Cancer. Observations were made in the neighbouring constellations Monoceros and Leo. Again, two objects were just slightly above the horizon (>20° altitude), because the YSOs are mainly near the galactic plane. The observation time was between 9:30 p.m. and 1:30 a.m. (UTC+2).

4.3 Observation on 20 April 2016

The list of objects observed on 20 April 2016 is given in table 5. The Moon was about 95% illuminated (two days before full moon) and its position was in the constellation

Object	Alternative name	Time	R.A.	Dec.
V* R Mon	NGC 2261, Hubble's Variable Nebula	21:50 - 23:30	06 39 09.95	+08 44 09.1
V* HK Ori		21:33 - 21:40	05 31 28.05	+12 09 10.3
Frosty Leo		0:14 - 1:23	09 39 53.96	+11 58 52.6

Table 4: Objects observed on April, 14 2016

Virgo. This resulted in a overall bright night sky, which is bad for observations. Because of the low positon of the galactic plane, all objects that were observed had an altitude lower than 30°, which again caused bad seeing conditions. The observation time was between 9:15 p.m. and 0:45 a.m. (UTC+2).

Object	Alternative name	Time	R.A.	Dec.
Red Rectangle	HD 44179	21:17 - 21:48	06 19 58.22	-10 38 14.7
CED 62	NGC 2163	22:00 - 22:30	06 07 49.5	+18 39 3
V* R Mon	NGC 2261, Hubble's Variable Nebula	22:50 - 22:55	06 39 09.95	+08 44 09.1
V* RY Tau		22:43 - 22:48	04 21 57.41	+28 26 35.6
V* XY Per		22:58 - 23:09	03 49 36.32	+38 58 55.6
V* V633 Cas	V* V376 Cas	23:19 - 0:01	00 11 25.83	+58 49 28.6
V* V628 Cas		0:20 - 0:45	23 17 25.58	+60 50 43.4

Table 5: Objects observed on April, 20 2016

4.4 Observation on 21 May 2016

The list of objects observed on 21 May 2016 is given in Table 6. Observation notes: The Moon was nearly completely illuminated (one day before full moon) and its position was in the constellation Libra. The overall night sky was bright, but no objects near the moon were observed. The images were taken in the second half of the night. By 4 a.m. in the morning, the brightened sky (due to the sun) interrupted the observation. The observation time was between 1:30 a.m. and 4:15 a.m. (UTC+2).

4.5 Information on the location of the observatory

The Observatorium Lustbühel Graz (OLG) is located at the east end of Graz (district Waltendorf).
Geographic position of the observatory [9]
Longitude: $-15°29, 7'$
Latitude: $+47°03, 9'$
Elevation: $484m$ above sea level

Object	Alternative name	Time	R.A.	Dec.
Parsamian 21		1:30 - 2:24	19 29 01	+09 38 4
V* PV Cephei		2:35 - 3:16	20 45 53.94	+67 57 38.7
V* V1982 Cyg	EM* LkHA 324	3:23 - 3:32	21 03 54.23	+50 15 10.0
GM1-27		3:39 - 3:43	20 20 13	+37 10 1
RNO 129		3:45 - 4:03	20 59 14.1	+78 23 04.0
V* V375 Lac	EM* LkHA 233	4:04 - 4:13	22 34 41.01	+40 40 04.5

Table 6: Objects observed on May, 21 2016

4.6 Determination of the optical layout and seeing conditions

4.6.1 Field of view

The field of view, or FOV, is limited due to the size of the CCD-chip and the focal length.
The FOV was determined by using 2 methods:

- Calculating the angle of view:

  Using the formula for calculating the angle of view for a lens projecting an image focused at infinity, one can determine the FOV:

$$\alpha = 2 \cdot \arctan \frac{d}{2 \cdot f}, \tag{3}$$

  with d the dimension of the CCD chip and f the focal length of the optical instrument. Using the data sheet of the camera STF 8300M, we get the size of 17.96 x 13.52 mm for the chip. [5] The focal length of the used telescope is given with f = 4500mm.

$$\Phi_\delta = 2 \cdot \arctan \frac{17.96}{2 \cdot 4500} = 0.2287° = 13.72' \tag{4}$$

$$\Phi_\alpha = 2 \cdot \arctan \frac{13.52}{2 \cdot 4500} = 0.1721° = 10.33' \tag{5}$$

  For the camera setup used for the observations, the result of (4) refers to length in the direction of the declination in arc minutes, while the result of (5) gives the size in direction of the right ascension.

  Additionally, the number of pixels per arc minute can be determined. With 3326 x 2504 pixel, one gets:

$$\Psi_\delta = \frac{3326}{13.72'} = 242.4\,pix/arcmin \tag{6}$$

$$\Psi_\alpha == \frac{2504}{10.33'} = 242.4\,pix/arcmin \tag{7}$$

The inverse values give the characteristic pixel size. Given in units of arcseconds per pixel:

$$\Phi = 0.248''/pix \tag{8}$$

- Determine the FOV with stellar coordinates (astronomic method):
  By comparing known coordinates of stars on an image and the corresponding pixel positions, the size of the FOV can be determined. For this purpose, we use an image of the object 'Red Rectangle' and use surrounding stars for the determination of the FOV. Since we do not expect distortions and only want to prove the calculated values, we use only two stars here.
  The image in Fig. 5 was taken on 20 April 2016 with 1x1 binning, i filter and an exposure time of 120 s. The size of the image is 3363 x 2543 pixels. The coordinate grid was produced using the service of the website nova.astrometry.net. The camera that is mounted on the telescope is not exactly aligned to north-south, but the coordinate grid of the figure shows that it does match pretty well. It is justified to use the x-axis as declination and the y-axis as right ascension in the following calculation.

  Coordinates of Star BD-10 1480:
  $RA = 6^h 20^m 15.0963^s$
  $\delta = -10°35'10.814''$
  in pixel (center of the star):
  $x = 1104 \pm 4$ pixel
  $y = 1796 \pm 4$ pixel

  Coordinates of Star BD-10 1475:
  $RA = 6^h 19^m 54.3820^s$
  $\delta = -10°43'27.495''$
  in pixel (center of the star):
  $x = 3082 \pm 4$ pixel
  $y = 585 \pm 4$ pixel

  Calculating the difference between both coordinates (declination in x-direction) leads to

  $\Delta x = 1978 \pm 8$ pixel, $\Delta\delta = 8.278'$
  $\Delta y = 1211 \pm 8$ pixel, $\Delta RA = 5.089'$ [1]

[1] The difference between the values of the right ascension was calculated and then converted to the

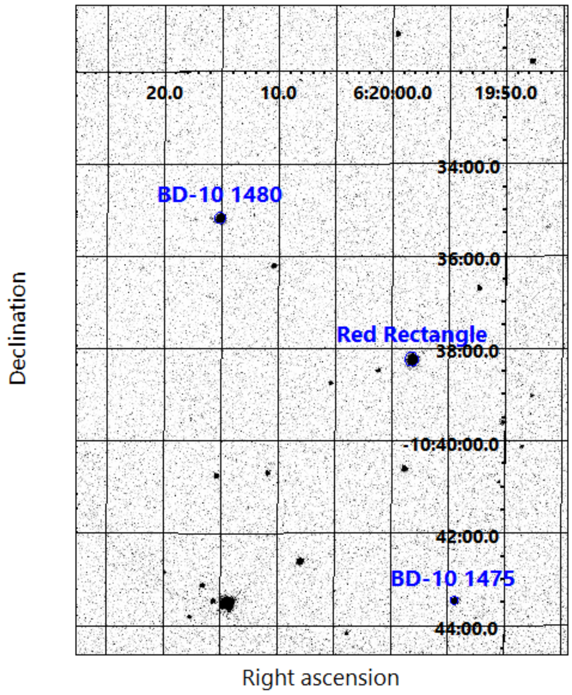

Figure 5: Image of the area surrounding 'Red Rectangle' in Leo. Taken at OLG on 20-4-2016.

Determining the number of pixel per arc minute:

$$\Psi_\delta = \frac{1978}{8.278'} = 238.9\, pix/arcmin \tag{9}$$

$$\Psi_\alpha = \frac{1211}{7.628'} = 237.9\, pix/arcmin \tag{10}$$

Considering errors by using the maximum error method, we get:

$$\Psi_\delta = (239 \pm 2)\, pix/arcmin, \Psi_\alpha = (238 \pm 3)\, pix/arcmin \tag{11}$$

Given in units of arcseconds per pixel:

$$\Phi_\delta = (0.251 \pm 0.002)''/Pix, \Phi_\alpha = (0.252 \pm 0.003)''/Pix \tag{12}$$

corresponding angle[°]. Because of the declination, the real size of this angle at the sky is less. Multiplying it with $cos(\delta)$, where δ is the average of the declination of both stars, brought this value.

These results deviate from the value using the first method only by $0.001''/Pix$. The values of the astronomic method will be used for measurements.

4.6.2 Determining the seeing

Astronomical seeing is caused by the earth's atmosphere when the light of a star moves through it. It causes rapidly changing speckle patterns instead of a steady diffraction pattern of a point source. When taking a long exposure image of a star, the seeing causes a so-called seeing disk.
For determining the seeing, we measure the full width at half maximum of a star's seeing disk (abbreviated: FWHM). An example of determining the seeing disk diameter is given here. We use an image of the object 'Red Rectangle' and use a star for measurement. The chosen star should not be saturated or in the non-linear regime.
The image in Fig. 6 was taken on 20 April 2016 with 1x1 binning, r filter and an exposure time of 120 s. The chosen star is designated as BD-10 1480 and its altitude was approx. 11°.
To get the FWHM, the counts along a line through the center of the seeing disk were evaluated using the program ds9. The counts as a function of the pixel range along this line are then plotted, which is shown in Fig. 7. The result resembles a gaussian. The FWHM is the width of the curve at the half height, which is plotted as a red line in the figure. The pixel size of this width is then converted to arcseconds.

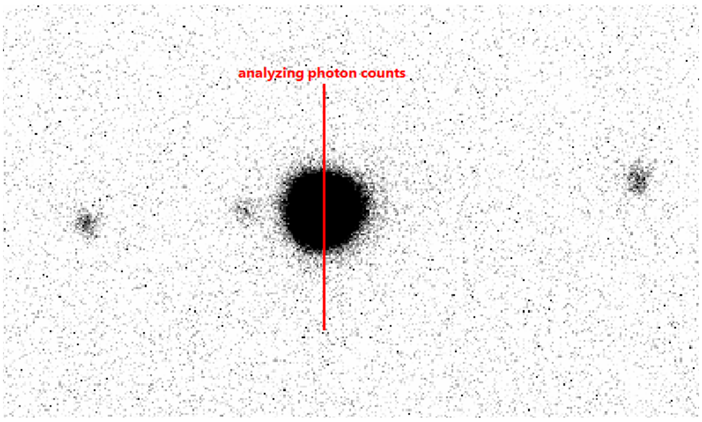

Figure 6: Analyzing the count number of the star. The counts along the red line were evaluated and plotted in Fig. 7.

We get the value $(3.54 \pm 0.05)''$ for the FWHM of the seeing disk. Considering the extremely low altitude (11°) of the object at the time of observation, we expected such a strong influence by astronomical seeing, resulting in suboptimal observing conditions.

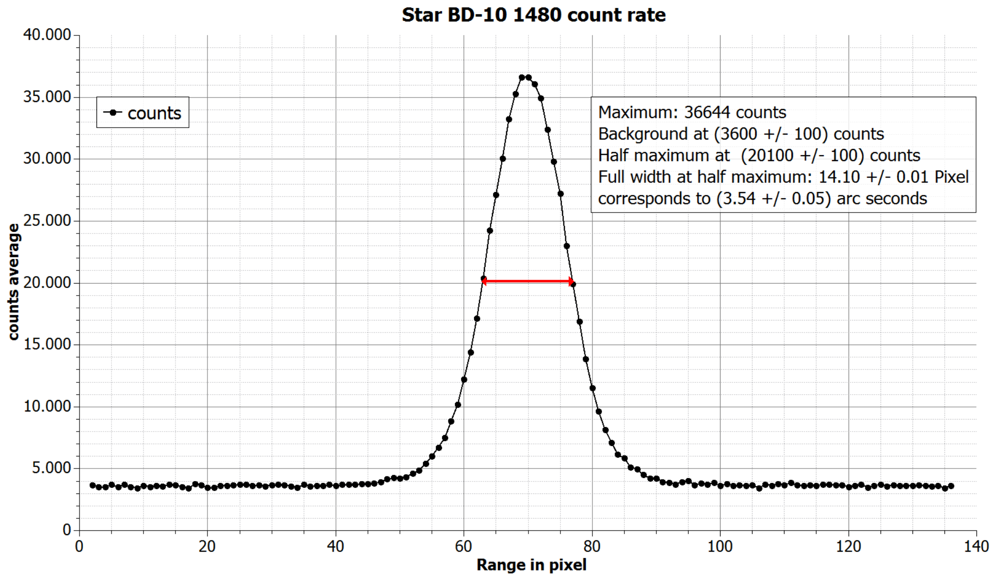

Figure 7: ADU counts of the star BD-10 1480. The red line indicates the full with at half maximum.

To further analyzing the seeing conditions of the observations, numerous seeing disk diameters were determined. They are listed in Table 7. The date of the observation and the altitude of the star are also given. Correlation between low altitude and large seeing disks can be identified.

4.6.3 Spatial resolution

The angular resolution is determined by the diameter of the primary mirror of a reflecting telescope. For a circular aperture, the Rayleigh criterion is used and is given by

$$\sin\alpha = 1.22\frac{\lambda}{D}, \tag{13}$$

where α is the resolution limit in rad, λ the wavelength and D the diameter of the telescope. Rewriting and expressing α in arcseconds leads to

$$\alpha = \arcsin(1.22 * \frac{\lambda}{D})[rad] = \frac{180 * 60 * 60}{\pi}\arcsin(1.22 * \frac{\lambda}{D})[arcsec] \tag{14}$$

With the small angle approximation $\sin\alpha \approx \alpha$ we get:

$$\alpha = \frac{180 * 60 * 60 * 1.22}{\pi}\frac{\lambda}{D} \tag{15}$$

Taking the value of 550 nm for λ (which is justified as our camera has the best quantum efficiency at 550 nm and the V filter is in this range) and the diameter of the primary

Observation Object	Date	exp. time	Alt	seeing disk
Frosty Leo	March, 17 2016	60s	50°	1.9”
NGC 2261	April, 14 2016	300s	25°	3.3”
HK Ori	April, 14 2016	120s	23°	4.0”
Frosty Leo	April, 15 2016	120s	29°	1.9”
Red Rectangle	April, 20 2016	120s	11°	3.5”
XY Per	April, 20 2016	240s	10°	4.5”
CED 62	April, 20 2016	360s	24°	2.5”
Parsamian 21	May, 21 2016	300s	41°	2.3”
PV Cephei	May, 21 2016	240s	60°	2.6”

Table 7: Determined seeing disks. Uncertainty: $\pm 0.5''$

mirror (0.5 m) we get:

$$\alpha = 0.277'' \tag{16}$$

The diffraction limit is undersampled considering the size of an arcsecond per pixel, but the camera is suitable even for good seeing conditions. We can conclude that the clear resolution of stars and objects depends mostly on the seeing conditions, as the FWHM of the seeing disks is about 5-20 times larger than the theoretical angular resolution.

5 Data reduction

With data reduction, one modifies the raw data of the images into form that is cleaned from instrumental (and atmospheric) effects. The raw data of the images have unwanted features like dark current, field curvature, hot pixels, cosmic rays etc. The images also have a (approx.) 10 pixels wide edge with a low count value. These pixels are purposely added and can be used to determine the bias.

To perform the data reduction, we need following images:
- The light frame, this is the image that holds the scientific information.

- Bias frame, this image is obtained by taking a image at zero seconds exposure time. This 'bias' is subtracted from the light frame.

- Dark frame, an image taken with a closed shutter with an exposure time equal to the exposure time of the light frames. It can be used to determine the signal originating from thermal electrons. As our camera has its own cooling unit, the dark frames were very similar to the bias frames and thus were not used in the data reduction.

- Flat frame. There are many ways to obtain a flatfield frame, usually by imaging an evenly illuminated object. Our used flatfields were sky-flats, produced by imaging the dusk sky. The flatfields have to be taken at the same temperature and the same filter as the light frames. The count values should reach about half of the CCD capacity with integration times of about 1 - 2 seconds. With the flatfields one can remove/diminish the effects of vignetting, dust and dirt inbetween the filter and the CCD chip and uneven sensitive CCD chip pixels. A flat frame for every used filter and every used binning is needed.

First, all bias frames and flat frames were combined to 'masterframes', using the median of all these frames. Then the data reduction perfomed with the following algorithm:

$$Newframe = \frac{(Lightframe - Biasframe)}{Flatframe} \tag{17}$$

The bias region was then cropped.
To further diminish the effects of hot or bad pixels, an IDL procedure called "sigma filter" was used, which replaces pixels that deviate from their neighbouring pixels by more than a specific standard deviation. It is replaced by the mean of the surrounding pixels.
When two or more images with long exposure times of an object (with the same filter and same binning) are taken, one can stack these images to get a better final result. To do that, a reference star was chosen for every observed object. The pixel coordinates of the center of the reference star was determined using the program ds9. The size of the final image was then chosen. The pixel range starting from the reference point to

the left and right (determining the size of the new image in the x-direction) and for up and down (determining the size of the new image in the y-direction) were chosen. With the reference coordinates for every picture and the length to the four borders of the new image, the images were stacked using a simple matrix addition in IDL. The new matrix with the stacked count values were then converted to a new image by using the 'writefits' routine in IDL. This stacking was performed on 13 of the observed objects.

The images in Fig. 8 display an example of the performed data reduction on an image of NGC 2261 with the r-filter.
In 8a the raw image is seen. It has two bias regions, numerous bad pixels, vignetting and artefacts.
In 8b the data reduction and a bad pixel removal was performed. As the flatfield was not perfectly created for this image, some of the artefacts are still there. Overall the image improved. The artefact removal as well as the bad pixel removal worked. The "halo" on the image is still slightly visible and the flatfield could not fully correct the varying background brightness, which was probably caused by the nearby moon.
In 8c a stacked image of the same object with 5 images is shown. This image is a zoom to show the nebula in more detail. Some parts of the artefacts due to dust on the filter are still visible. Nonetheless, the structure of the nebula got much clearer. Almost no hot pixel is visible.

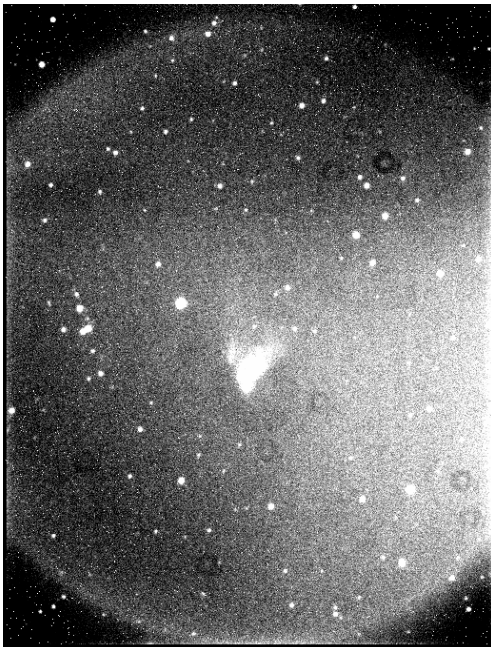

(a) NGC 2261 raw image with r-filter, exposure time 300 s. Error due to vignetting is about 1500 counts. The high background illumination on the right side of the image is probably caused by the nearby moon.

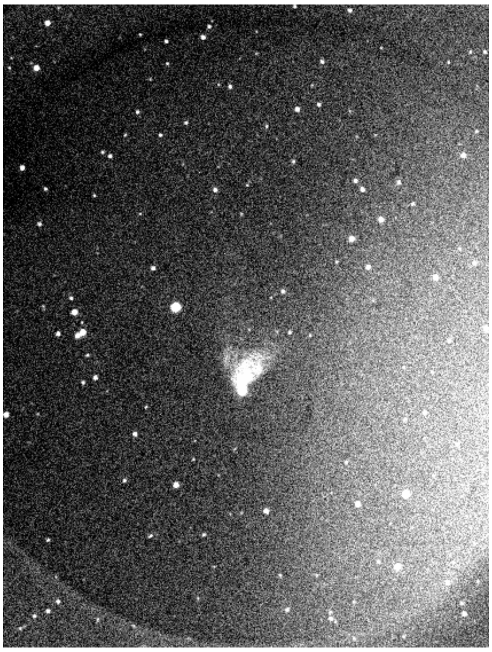

(b) Reduced image. Error due to vignetting is about 200 counts, it got much better. However, the flatfield could not correct the illumination on the right side of the image caused by the nearby moon.

(c) Cropped and stacked frame of numerous NGC 2261 images. This images is a zoom to show the nebula in more detail.

Figure 8: Example of data reduction on NGC 2261

6 Analysis

In this chapter, the observed objects are shown and their properties are further analyzed. For this purpose, various sources are used for comparison with our data. Data reduction and photometric enhancements are already performed on the displayed images (see 5).
The objects are mainly YSOs, with only the last two described objects (Red Rectangle and Frosty Leo) being protoplanetary nebulae. Except it is stated otherwise, north is upwards and west is to the right in all images. The images are cropped to show the nebulae in detail. All RGB images were made from the V, r and i filters with SAOimage ds9.

The following abbreviations are used in the Figure descriptions:

Exp.time ... Exposure time of the image
Stack. ... Image consisting of two or more stacked images with further information on exposure times
Bin ... Binning of the image, used binning modes are 1x1, 2x2 and 3x3
Scale ... scaling details and cutoff limits
lin ... linear scaling
log ... logarithmic scaling
max ... overall maximum count a pixel has in the displayed image
bckgr ... count value of the image's background, refering to the starless regions (with uncertainty)

6.1 NGC 1555, Hind's Nebula

Object observed: 17 March 2016

NGC 1555, also known as Hind's Nebula or Hind's Variable Nebula (named after its discoverer John Russel Hind), is a reflection nebula illuminated by the star T Tauri. The star is the prototype of the T Tauri type stars, which are pre-main-sequence stars with masses between 0.2 and 2 $M_\odot$ (see 3.1). As observations have shown, T Tau is actually a triple star system with two companion stars visible in the infrared ([10]Köhler et al. 2016).
The object was observed with B, V, r and i filters.

With B-filter, the nebula appeared extremely faint and therefore was not used for the RGB image.
Combining the other 3 images to one RGB image, where i appears as red, r appears as green and V appears as blue lead to the result seen in Fig 12.

The elliptical shape of the surrounding stars in East-West direction is a consequence of imperfect tracking. The nebula appeared very clear in infrared, while it is hard to see in the visual band. The star itself does not appear stellar, as there is a continuation towards north-west (also seen in images of the DSS POSS2/UKSTU images). The nebula itself is located 0.5' to the west of T Tauri. It extends out to a sharp

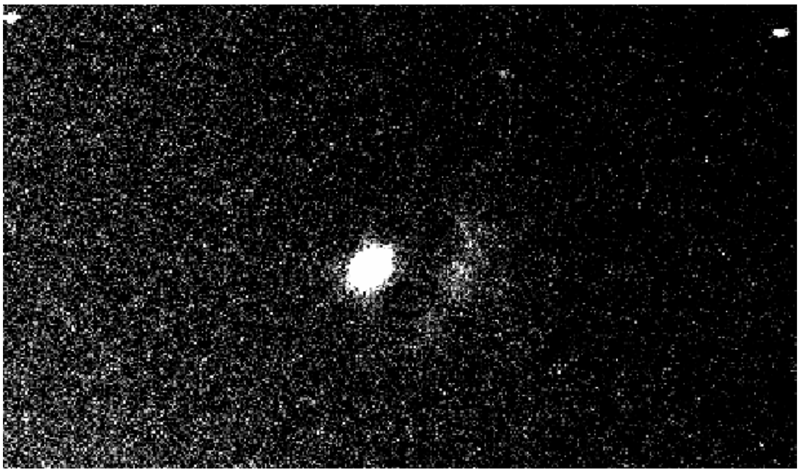

Figure 9: NGC 1555 in V-Band. Stack: (120 + 180 + 300)s, Bin: 3x3, scale: lin, 40000-49072, max: 188000, bckgr: 41700 ± 400

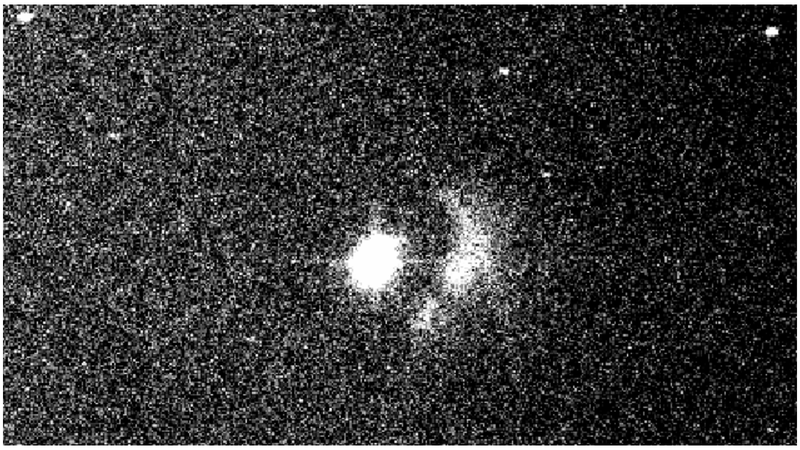

Figure 10: NGC 1555 in r-Band. Stack: (60+ 2x120 + 300)s, Bin 3x3, scale: lin, 47100-57216, max: 253600, bckgr: 48300 ± 200

end in the north (with an unclear split), while it splits in two parts towards south. The eastermost southern part is divided by a gap, which is not visible on the STScI Digitized Sky Survey images. Farther away from the star the nebula fades out.

Considering only this bright, visual part, the apparent size of the nebula is 1.3' (Dec) and 0.2'-0.4' (RA). The distance to the T Tau star system is given by 147.6 ± 0.6 pc ([11]Loinard et al. 2007). As this is an estimate, the uncertainties are not considered. For the nebula NGC 1555 we get the size of 0.18 Ly (Dec) and 0.04 Ly (RA). Given in AU: 11500 AU (Dec) and 2650 AU (RA).

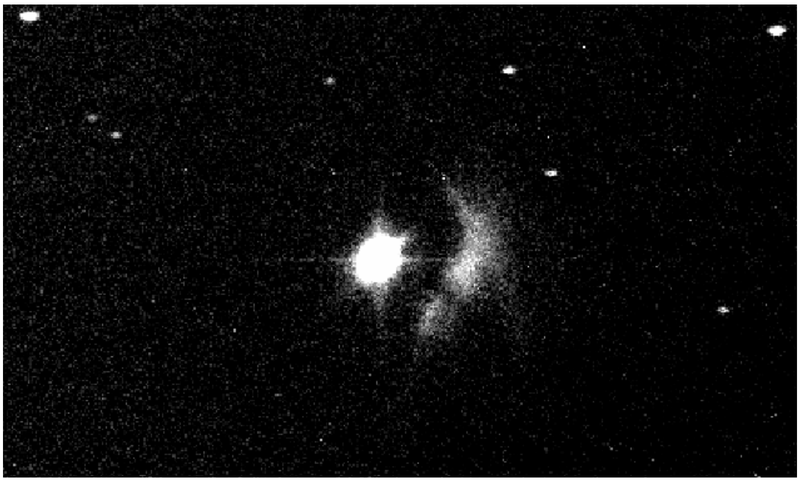

Figure 11: NGC 1555 in i-Band. Stack: (5x120 + 180 + 300)s, Bin: 3x3, scale: lin, 28744-36859, max: 465000, bckgr: 28700 $\pm$ 100

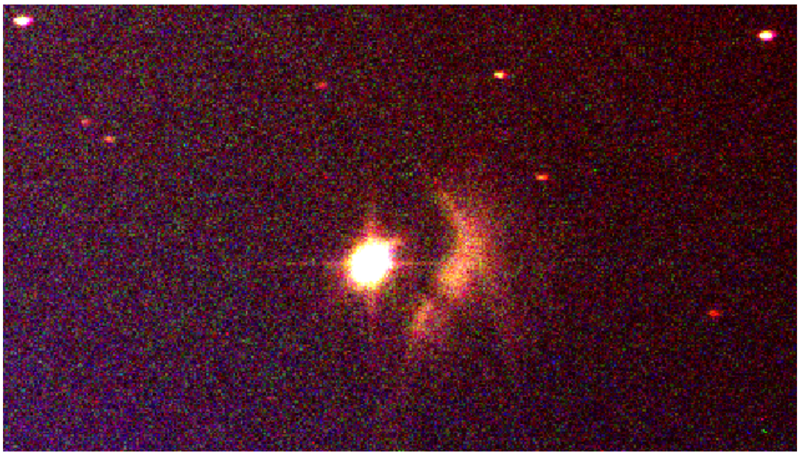

Figure 12: NGC 1555 as color-composite

6.2 AB Aur

Object observed: 17 March 2016

AB Aur is a Herbig Ae/Be star in the constellation Auriga. The star has an associated reflection nebula east of it. The object was observed with the filters B, V, r and i.
Fig. 13 shows the object in all filters. In all images the star AB Aur is saturated. The extension to the north of the star is clearly visible in all filters, while no extension to

the west is visible. Here, the 3x3 binning may not the be the best option, as a possible separation between the star and the nebula would have been clearer and the nebula is already clearly above the background. The binning was chosen to get additional structures of the nebula in the surrounding area, which did not work. Only the bright inner part of the nebula got visible. On the other hand, the bad tracking and the low altitude played a big negative role in imaging the nebula. Under these conditions, these pictures were the best possible result.

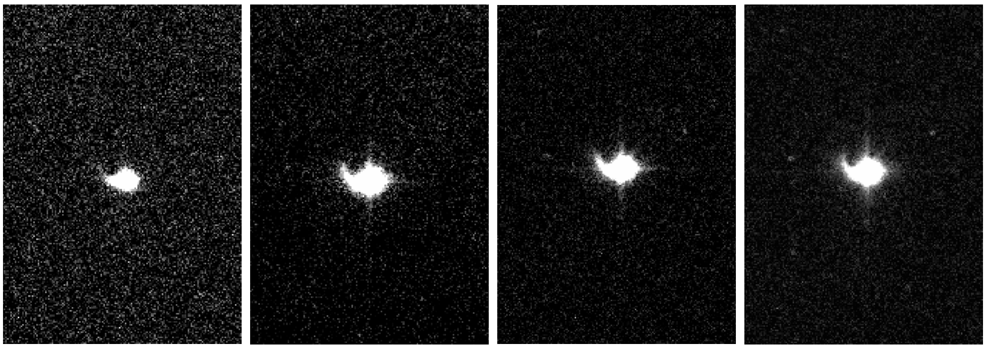

(a) Ab Aur in B-Band. Exp.time: 120 s, Bin: 3x3, scale: lin, 2340-5600, max: 65000, bckgr: 2360 ± 20

(b) AB Aur in V-Band. Exp.time: 120 s, Bin: 3x3, scale: lin, 11700-18600, max: 65000, bckgr: 11900 ± 100

(c) AB Aur in r-Band. Exp.time: 120 s, Bin: 3x3, scale: lin, 12900-22000, max: 65000, bckgr: 12960 ± 50

(d) AB Aur in i-Band. Exp.time: 120 s, Bin: 3x3, scale: lin, 4270-15000, max: 65000, bckgr: 4300 ± 30

Figure 13: AB Aur in different filters

6.3 Holoea

Object observed: 17 March 2016

The object Holoea (or IRAS 05327+3404) is a young stellar object (YSO) located in the open cluster M36 in Auriga, although it may not be a part of it. It is classified as a star that is on the transition between the Class I and Class II phase of the stellar evolution. Its distance is not exactly known and is given from 1.2 kpc (distance of M36) up to 1.6 kpc ([12]Morata et al. 2013).
According to SIMBAD, the object is very faint in the V filter with 18.62 mag and appears much brighter in the infrared. It was not expected to see Holoea in the V-band. Observations in the i band was more promissing. Observations were made with V, r and i.

The red circle indicates the position of Holoea.
Holoea appears to be an object that is on the edge for detection with the telescope at

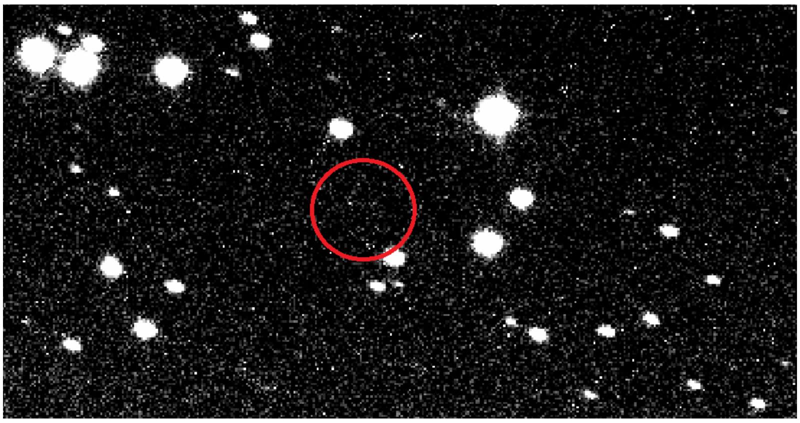

Figure 14: Holoea in V-Band. Exp.time: 180 s, Bin: 3x3, scale: lin, 17000-21000, max: 65000, bckgr: 17200 ± 300

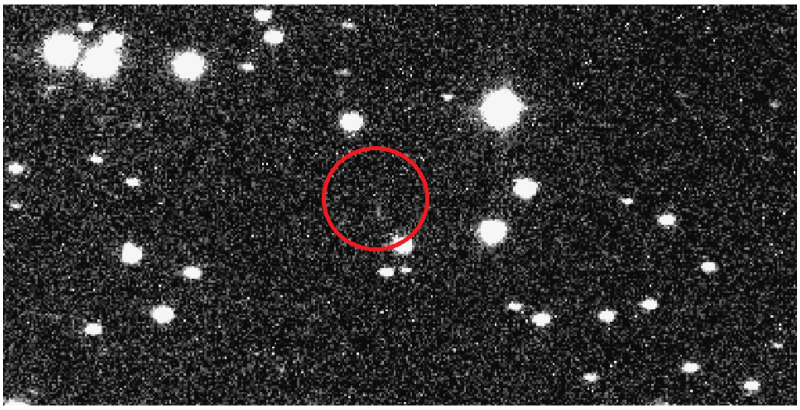

Figure 15: Holoea in r-Band. Exp.time: 180 s, Bin: 3x3, scale: lin, 18000-19200, max: 65000, bckgr: 18000 ± 300

OLG. Long exposure times and stacking in the i- or r-band could expose more details. As expected, the object was not visible in V (Fig. 14). A small band expanding to the north is observable in r (Fig. 15), in i we see a stellar like object at the position of Holoea and a diffuse spot to the north of it (Fig. 16).
A colored DSS image of Holea is presented in Fig.17.

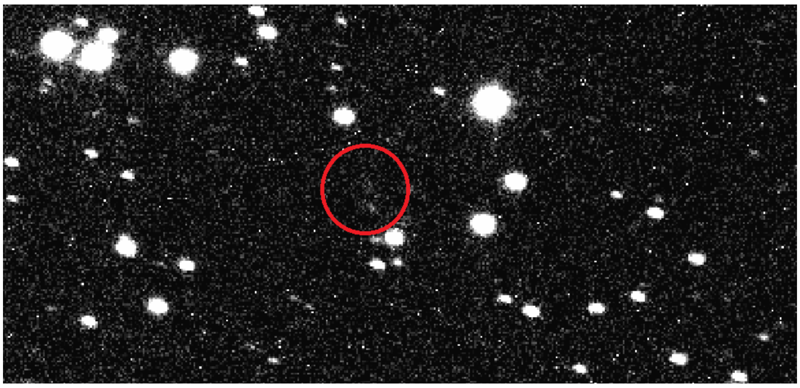

Figure 16: Holoea in i-Band. Exp.time: 180 s, Bin: 3x3, scale: lin, 6300-7300, max: 65000, bckgr: 6200 ± 200

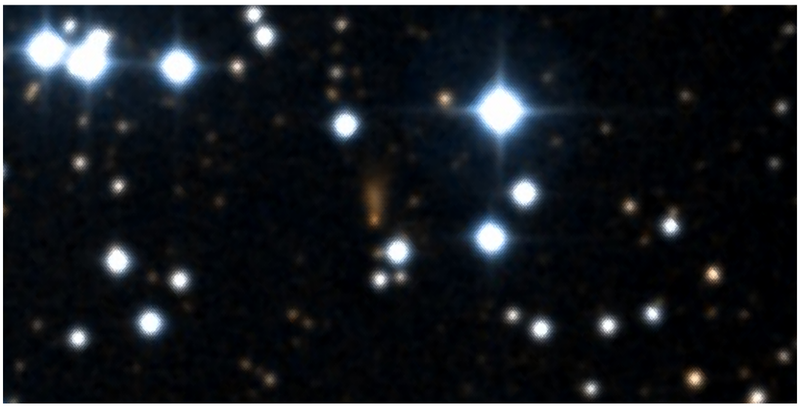

Figure 17: Color image of Holoea. Credit: Digitized Sky Survey - STScI/NASA, Colored & Healpixed by CDS [13]

6.4 FU Ori

Object observed: 17 March 2016

The star FU Orionis is the prototype star of the FU Orionis class objects, which are highly variable pre-main sequence stars that show extreme magnitude and spectral type changes. The star had a flare up in the years 1936 to 1937, changing the visual brightness by approx. 6 mag ([14] [15]Herbig 1977, Hartmann 1985). Now it has a visual brightness of 9.6 mag [8]. It is surrounded by a reflection nebula, having a crescent shape (nearby) southwest of the star and expanding to the north and east. Observations were made with the filters B, V, r and i.

The response in B was very weak, no nebula visible. In V (Fig. 18b), the closest

part of the nebula is visible as a crescent shape that fades out in the southeast and northwest direction. The area northeast of the star has a higher number count as the surrounding area, but this falls into the uncertaincy as the image is not even illuminated. This problem was caused by the nearby moon.
The observation in r (Fig. 18c) brought the same conclusion, although the shape is less clear here. In both figures of V and r contours were used to emphasize the structure. As the nebula is very close to the star, the structure is not that clear visible. The image in i (Fig. 19) could not be scientifically evaluated as something caused a problem in the optical observation. In i, all brighter stars clearly appear distorted along the diagonal of the image. As the object was only approx. 10° above the horizon, it is possible that an antenna (or another object in the line of sight) caused the distortion. Another possibility would be that the tracking of the dome did not work properly and the cupola edge of the slit caused the problem.

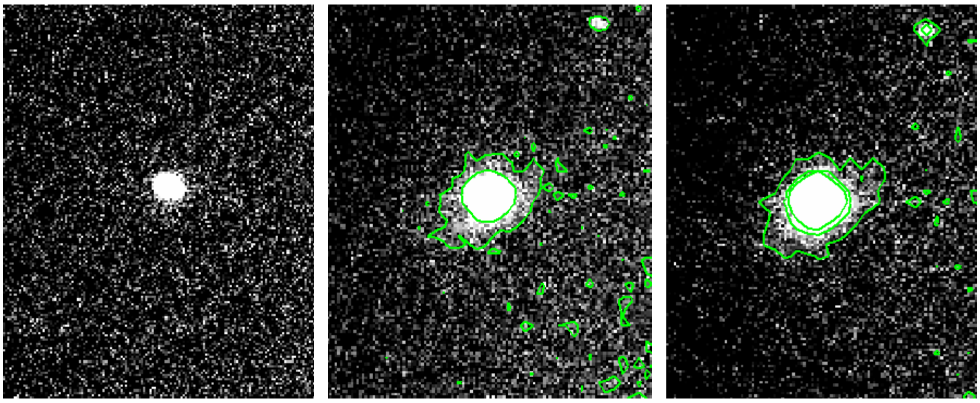

(a) FU Ori in B-Band. Exp.time: 120 s, Bin: 3x3, scale: lin, 4000-4700, max: 26000, bckgr: 4300 ± 50

(b) FU Ori in V-Band. Exp.time: 120 s, Bin: 3x3, scale: lin, 22150-23700, max: 65000, bckgr: 22600 ± 300

(c) FU Ori in r-Band. Exp.time: 120 s, Bin: 3x3, scale: linear, 24610-27000, max: 65000, bckgr: 25000 ± 300

Figure 18: FU Ori in different filters

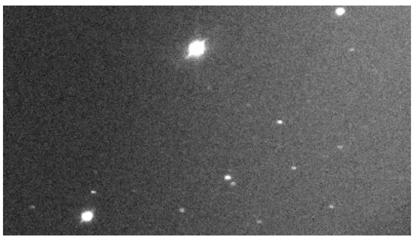

Figure 19: FU Ori in i-band (bright object above the center). The distortion along the diagonal of the image is also visible for the birght star in the lower left

6.5 NGC 2261, Hubble's Variable Nebula

Object observed: 17 March 2016, 14 April 2016, 20 April 2016

NGC 2261 (also called Hubble's Variable Nebula or Caldwell 46) is a highly variable reflection nebula illuminated by the Herbig Ae/Be star R Mon in the constellation Monoceros. The name "Hubble's Variable Nebula" was assigned because Edwin P. Hubble extensively studied the variable properties of the nebula ([16]Hubble 1916). The comet-shaped object changes its appearance over the course of months and weeks. A possible explanation for the rapid changing features would be dust moving around the star and casting shadows on the nebula ([17]Johnson 1966). The object is very rewarding in terms of brightness and changing structures. Even with linear Min-Max scaling, the nebula and its features are clearly visible. The object was observed with the filters B, V, r and i on 17 March, 14 and 20 April 2016.

The following images (Fig. 20)were taken on 14 April 2016 with 2x2 binning. MinMax scaling is used and several long exposures are stacked. The image with filter B is not included as again the response was very weak and the tracking got worse close to the horizon (stars were elongated after 5 min exposure).

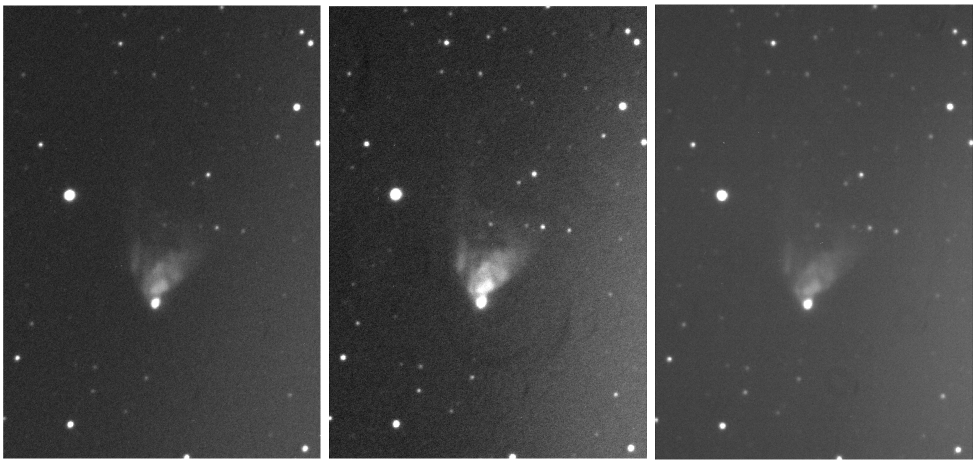

(a) V-Band, Stack: (5x300 + 120)s, scale: lin, 120000-381900 (min-max), bckgr: 124000 ± 1500

(b) r-Band, Stack: 4x300 s, scale: lin, 98420-254800 (min-max), bckgr: 102000 ± 1500

(c) i-Band, Stack: 3x300s , scale: lin, 29000-192800 (min-max), bckgr: 30800 ± 800

Figure 20: NGC 2261 in different filters with Bin: 2x2 and linear min-max scaling.

Fig. 21 shows how the nebula changed between 17 March and 14 April. Notably, a dark spot in the nebula, which was 22" to the north of the star R Mon on the 17 March, seems to have changed its position to the east, taking the postion of 30" to the northeast of R Mon on 14 April. This shadow moved $9 \pm 4''$ within 28 days. Observations on the 20 April 2016 further showed the progression of the dark spot,

shadowing more of the lower part of the detached nebulosity in the northeast. On the other hand, the detachment itself is also a moving shadow through the nebula, so the moving observation might be more complex. The measured movement will be discussed later on. The brightest spot in the nebula above the star also altered its form, changing into two bright spots on 14 April.
The two images of Fig. 21 are again shown in Fig. 22 with contouring lines to further indicate the structure details of the innermost part of NGC 2261.

(a) NGC 2261 on 17 March 2016. r-band, Stack: 3x120 s, Bin: 3x3.

(b) NGC 2261 on 14 April 2016. r-band, Stack: 4x300 s, Bin: 2x2

Figure 21: NGC 2261 at two different observation dates

A colored RGB image of NGC 2261 (ranging from infrared to visual) is shown in Fig. 23. The images of 20 were used in this colour-composite.

We can see in the coloured image that the comet shaped nebula expands with its eastern nebulosity patch far into the north with a size of approx. 3'. The visible expansion in the RA is approx. 1.5'.
The star R Mon is not directly visible as it is surrounded by a nebulosity. This fact makes distance estimates challenging, as the parallax or stellar propertes cannot be measured. The nebula lies less than 1° away from the object NGC 2264 (Cone Nebula and Christmas Tree Cluster) and thus the distance of 800 pc of NGC 2264 is frequently used for R Mon ([18]Jones and Herbig 1982). Recent estimations had the value of 760 pc ([19]Close et al, 1997), which are used here. With this distance, we get a size of 0.66 pc (dec.) and 0.33 pc (RA) of the nebula. To further discuss the motion of shadows in the nebula, this distance yields a motion of $(4.23 \pm 1.8)10^8 \frac{m}{s}$ of the shadow. The speed of light is within this uncertainty, which is no surprise as shadows move with c. Similar observations were made by Lampland 1931 where the shadows moved 1/4" per day, which yields the speed of light at about 750 pc ([17]Johnson 1966).

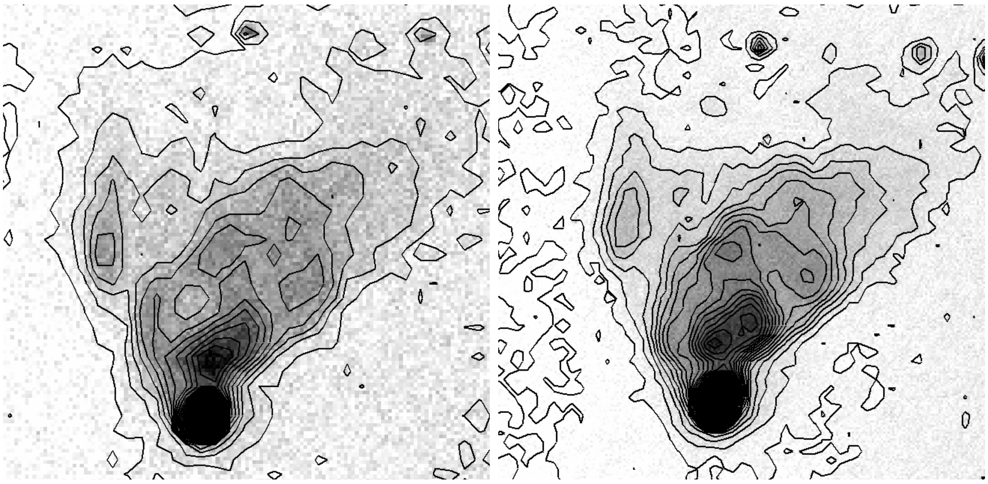

(a) NGC 2261 on 17 March 2016. r-band, Stack: 3x120 s, Bin: 3x3
(b) NGC 2261 on 14 April 2016. r-band, Stack: 4x300 s, Bin: 2x2

Figure 22: NGC 2261 (inverted) at two different observation dates with contour plots

Figure 23: RGB image of NGC 2261 from 14 April 2016 (i-filter as red, r-filter as green, V-filter as blue). In this image, north is to the left and west is upwards.

6.6 HK Ori

Object observed: 14 April 2016

HK Orionis is classified as a Herbig Ae/Be star in the constellation Orion. It is a young binary system. The nearby reflection nebula around HK Ori was observed. As it appears blue on the DSS images, observations were made with the filters B and V.

Figure 24: HK Ori in V-Band. Exp.time: 120 s, Bin: 3x3, scale: lin, 24200-25360, max: 65000, bckgr: 24700 ± 200

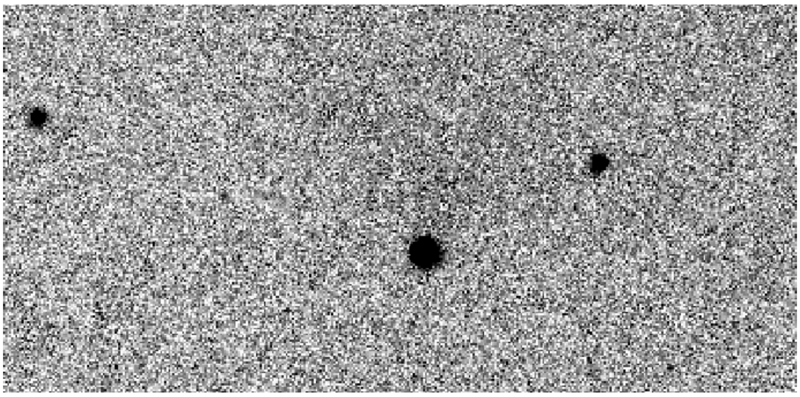

Figure 25: HK Ori in B-Band, inverse colors to enhance the contrast. Stack: 2x180 s, Bin: 3x3, scale: lin, 10321-11061, max: 110000, bckgr: 10570 ± 20

No nebula is visible in the V band (24). Fig. 25 is a stacked image of two long exposures with the B filter. Here, the supposed area of the nebula is about 50 counts higher than the background, which is close to the uncertainty but nonetheless significantly higher than the background. Without the stacking, the nebula would be indistinguishable from the background. For comparison purposes, the colored DSS image of HK Ori is presented (Fig. 26).

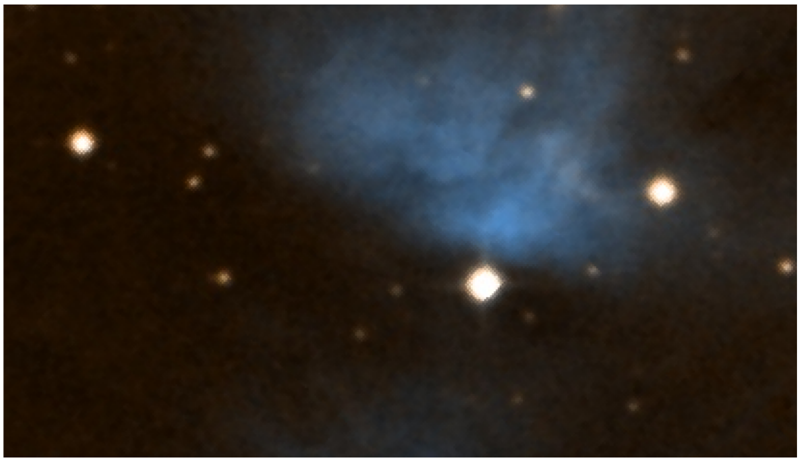

Figure 26: Color image of HK Ori. Credit: Digitized Sky Survey - STScI/NASA, Colored & Healpixed by CDS [13]

6.7 CED 62

Object observed: 20 April 2016

CED 62, also known as NGC 2163, is a bipolar reflection nebula in the constellation Orion. The object was observed with the filters B, V, r and i.
The color image in Fig 28 does not include the B-band image, because the overall response with the B-filter is relatively weak, although the nebula is clearly visible. The bipolar nature of the nebula is visible in all filters (Fig. 27). The northern part is clearly brighter than the southern part.

6.8 RY Tau

Object observed: 20 April 2016

RY Tau is a T Tauri type star with a reflection nebula in the constellation Taurus.
The object was observed in the r-band.

There appears to be no visible nebula in the image shown in Fig. 29a. There is, however, a measurable difference in number counts where the nebula should be and its surrounding area. The difference is about 100 counts on the eastern patch of the nebula and 50 counts on the nebula that should surround the star and face to the north and west. This difference is less than the standard deviation of the background, so this could also be the result from artefacts in the image. A stacking of images could provide a solution (the stars are, however, already saturated). Fig. 29b displays an image from the DSS for comparison.

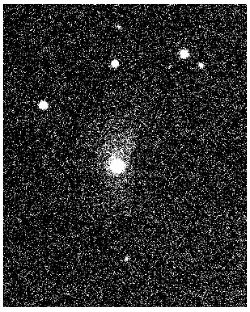

(a) CED 62 in B-Band. Exp.time: 360 s, Bin: 3x3, scale: lin, 10700-12600, max: 65000, bckgr: 11170 ± 50

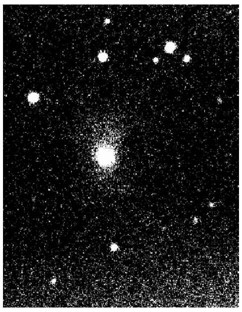

(b) CED 62 in V-Band. Exp.time: 300 s, Bin: 3x3, scale: lin, 40000-43430, max: 65000, bckgr: 40700 ± 100

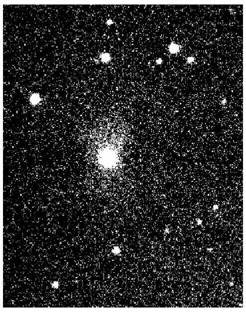

(c) CED 62 in r-Band. Exp.time: 240 s, Bin: 3x3, scale: lin, 36300-38000, max: 65000, bckgr: 37000 ± 200

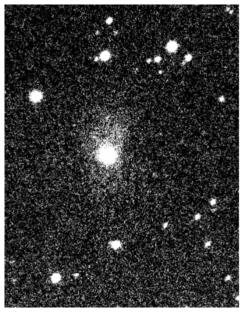

(d) CED 62 in i-Band. Exp.time: 300 s, Bin: 3x3, scale: lin, 14345-17800, max: 65000, bckgr: 14950 ± 50

Figure 27: Ced 62 in different filters

Figure 28: CED 62 as color-composite. The i-filter (red) is combined with the r-filter (green) and the V-filter (blue).

6.9 XY Per

Object observed: 20 April 2016

XY Per is a Herbig Ae/Be star with a reflection nebula in the constellation Perseus. The object was observed with the filters B, V and r.

As seen in Figs. 30a - 30c, the nebula is not visible. It should lie close to the 9.8 mag bright star XY Per (in the middle of the picture) towards southwest with a faint nebulosity around the whole star. The 2x2 binning was chosen for the B and V band to resolve the edge of the nebula in the southwest. A 3x3 binning could have been

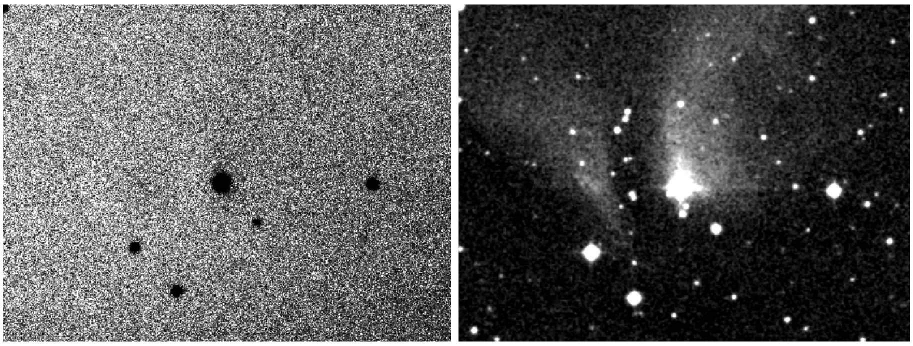

(a) RY Tau in r-Band. Inverted for contrast purposes. Exp.time: 120 s, Bin: 3x3, scale: lin, 25560-26980, max: 65000, bckgr: 25800 ± 100

(b) RY Tau from the digitised sky survey DSS (POSSII-N)

Figure 29: RY Tau comparison between OLG and DSS image

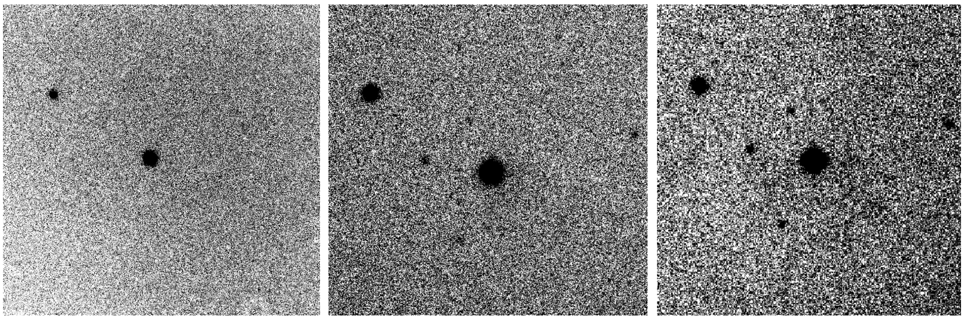

(a) XY Per in B-Band. Exp.time: 300 s, Bin: 2x2, scale: lin, 3880-4430, max: 17000, bckgr: 4200 ± 50

(b) XY Per in V-Band. Exp.time: 240 s, Bin: 2x2, scale: lin, 15200-16000, max: 65000, bckgr: 15610 ± 50

(c) XY Per in r-Band. Exp.time: 180 s, Bin: 3x3, scale: lin, 26430-27540, max: 65000, bckgr: 26800 ± 100

Figure 30: XY Per in different filters. Inverted color for contrast purposes

better to detect any nebulosity at all. The area of the nebula is within sigma, but somewhat above the background in terms of countrate in all three images.
The image of the DSS is provided for comparison (Fig. 31).

6.10 V633 Cas and V376 Cas

Object observed: 20 April 2016

V633 Cas and V376 Cas are two Herbig Ae/Be stars with reflection nebulae lying very close to each other in the constellation Cassiopeia.

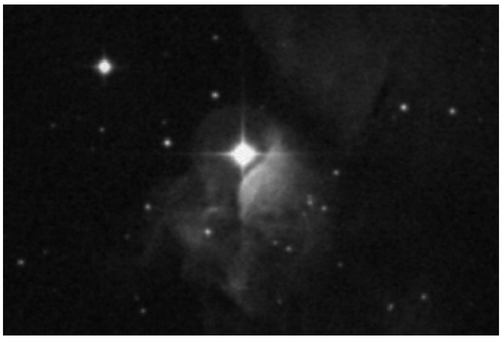

Figure 31: XY Per from the (POSSII-J)

The objects were observed with the filters V, r and i.

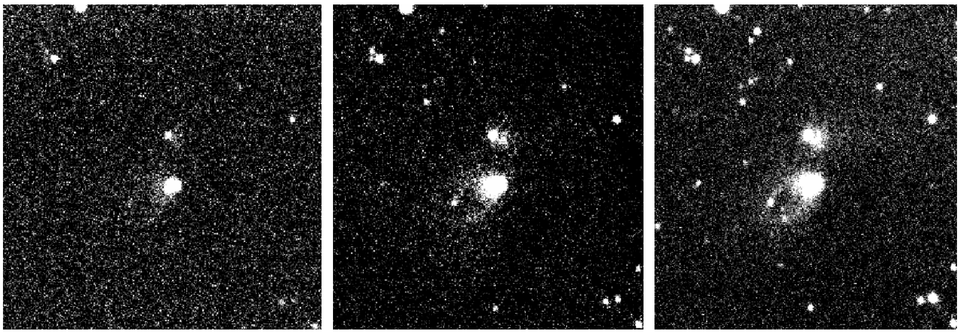

(a) V633 Cas and V376 Cas in V-Band. Exp.time: 300 s, scale: lin, 2600-28270, max: 45000, bckgr: 26150 $\pm$ 150

(b) V633 Cas and V376 Cas in r-Band. Stack: (120 + 240 + 360)s, scale: lin, 61770-66850, max: 130000, bckgr: 62200 $\pm$ 100

(c) V633 Cas and V376 Cas in i-Band. Stack: (300 + 420)s, scale: lin, 29200-35140, max: 110000, bckgr: 29600 $\pm$ 100

Figure 32: V633 Cas and V376 Cas in different filters. Bin: 3x3

The images Figs. 32a - 32c show the nebulae. V633 Cas is the southern star with a ring-shaped reflection nebula facing southeast. V376 Cas is the northern star with its reflection nebula facing west. The stacked image in the i-Band (Fig.32c) brought the best result with the V633 Cas loop clearly visible. The 3 stars visible within the loop are probably field stars ([20]Asselin et al. 1996). There is a faint nebulosity suspected reaching 1' to the west of V376 Cas, beyond the compact nebula closeby. Additionally, the nebulae were observed with the binning 2x2 and 1x1, but without revealing more structure.
Fig. 33 shows the RGB image consisting of the images shown in Fig. 32.

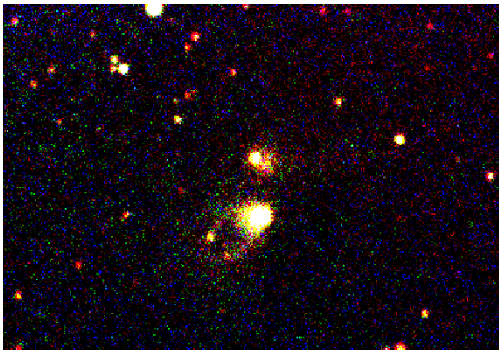

Figure 33: RGB image of V633 Cas and V376 Cas (i-filter as red, r-filter as green, V-filter as blue)

6.11 V628 Cas

Object observed: 20 April 2016

V628 Cas (MWC 1080) is a variable Herbig Ae/Be star with reflection nebula in the constellation Cassiopeia.
The object was observed with the filters V, r and i.

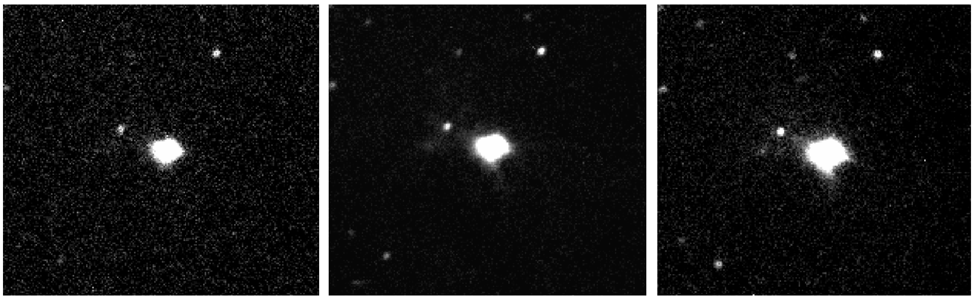

(a) V628 Cas in V-Band. Exp.time: 420 s, scale: lin, 18600-29600, max: 65000, bckgr: 18750 ± 50

(b) V628 Cas in r-Band. Stack: (120 + 180 + 240 + 420)s, scale: lin, 71400-155000, max: 310000, bckgr: 71100 ± 200

(c) V628 Cas in i-Band. Exp.time: 240 s, scale: lin, 9420-23550, max: 65000, bckgr: 9800 ± 50

Figure 34: V633 Cas and V376 Cas in different filters. Binning: 3x3

The images Figs. 34a - 34c show the object. The nebula around the star is very bright and compact, with tips to the west and south. To the east, a faint nebulosity is visible in r and i, with detached patches near the fainter star.
Fig. 35 shows the RGB image composed of the images shown in Fig. 34.

Figure 35: RGB image of V628 Cas (i-filter as red, r-filter as green, V-filter as blue)

6.12 Parsamian 21

Object observed: 21 May 2016

Parsamian 21 is an object with a reflection nebula in the constellation Aquila. The Star HBC 687 is classified as a FU Ori [8]. The distance is estimated with 400pc ([21]Kóspál et al. 2008).
The object was observed with the filters B, V, r and i.
In Fig. 36 the images with 3x3 binning are shown. The image in rstacked (3x300 s + 1x180 s) The r-band was chosen for the stacking, the nebula was very clear in r. Except for the B-band, the comet like shape of the nebula is clearly visible in all filters. It appears that the nebula has two tails facing north, with the western tail clearly more visible than the eastern part. Both tails merge to one nebulosity about 42" northwest of the illuminating star, resembling an elliptical "hole" in the nebula.
A RGB composite is shown in Fig. 37. The red color of some surrounding stars is clearly visible.

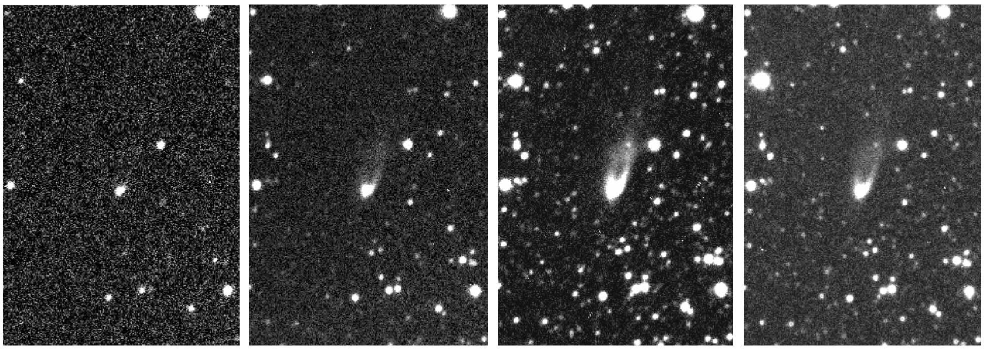

(a) Parsamian 21 in B-Band. Exp.time: 180 s, scale: lin, 3000-4890, max: 20000, bckgr: 3400 ± 10

(b) Parsamian 21 in V-Band. Exp.time: 180 s, scale: lin, 11000-20300, max: 65000, bckgr: 11350 ± 50

(c) Parsamian 21 in r-Band. Stack: (3x300 + 180)s, scale: lin, 61900-81500, max: 260000, bckgr: 63100 ± 100

(d) Parsamian 21 in i-Band. Exp.time: 180 s, scale: lin, 4700-13000, max: 65000, bckgr: 4850 ± 50

Figure 36: Parsamian 21 in different filters. Bin: 3x3

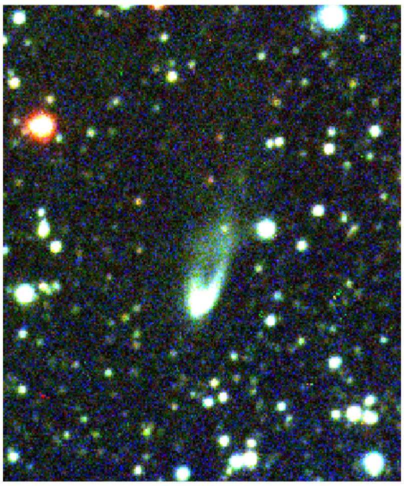

Figure 37: RGB image of Parsamian 21 (i-filter as red, r-filter as green, V-filter as blue)

6.13 PV Cep, Gyulbudaghian's Nebula

Object observed: 21 May 2016

PV Cep is the illuminating star of Gyulbudaghian's Nebula in the constellation Cepheus. Both star and nebula are highly variable, with PV Cep changing its apparent brightness by up to 4 - 5 mag. The pre-main sequence star is classified as a variable star of Orion type [8] and as Herbig Ae/Be star ([22]Arce et al. 2002). Its distance is reported

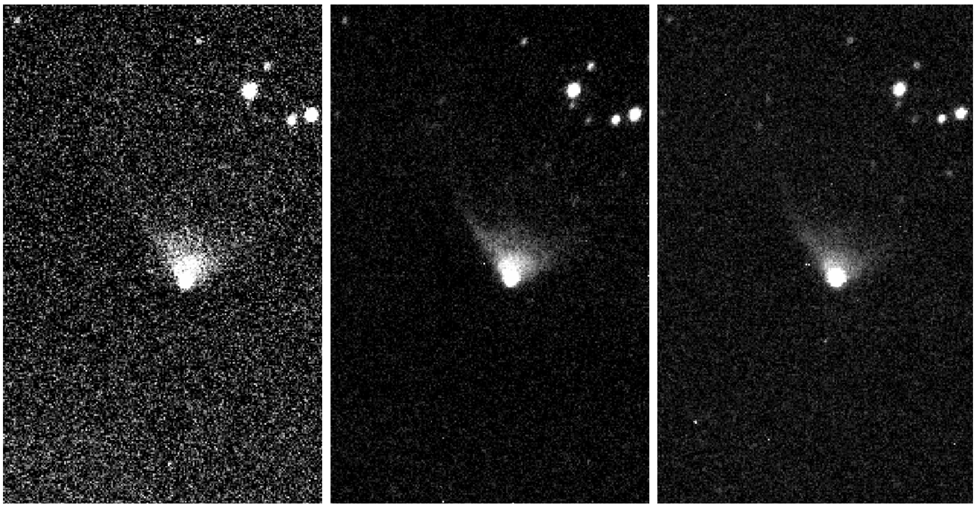

(a) PV Cep in V-Band. Exp.time: 240 s, scale: lin, 7500-8700, max: 16000, bckgr: 7960 ± 40
(b) PV Cep in r-Band. Stack: (240 + 300)s, scale: lin, 16500-19300, max: 41000, bckgr: 16550 ± 50
(c) PV Cep in i-Band. Exp.time: 240 s, scale: lin, 3000-5300, max: 23000, bckgr: 3150 ± 10

Figure 38: PV Cep in different filters. Bin: 3x3

to be about 325 pc ([23]Straizys 1992) up to 500 pc ([22]Arce et al. 2002).
The object was observed in V, r and i filters.

As is seen in Fig. 38, the nebula extending to the north is clearly visible in all three filters. The overall form of the nebula looks similar to NGC 2261, with the star sitting in the south of it and illuminating the triangle-shaped nebula.
In Fig. 39a a color image reaching from infrared to V-band is given. In 39b, a stacked image of the nebula is used to estimate the brightness of the star in the i-band. The image has a 2x2 binning, making the measurement more accurate than for the 3x3 binning. Three (not saturated) stars in the image and their brigthness in the I band (according to Simbad) were used for the photometry. Their I- brightness and determined sum of photon counts are given in Tab. 8. The sum was determined by summing up all counts in a circle comprising the star and then subtracting the sum of the background within a circle of the same size. This method works for stars without surroundign nebula. For PV Cep, we can assume that the real brighthness would be less, as we get a higher sum over counts due to the nebula. This results in a high uncertainty for the value. To calculate the brightness in mag, the equation

$$m_{PVCep} = 2.5 \cdot \log \frac{N_{star}}{N_{PVCep}} + m_{star} \tag{18}$$

was used. Here, m_{PVCep} is the brightness of PV Cep in mag, m_{star} the brightness of a surrounding star in mag, N_{PVCep} the sum over all counts of PV Cep and N_{star} the sum over all counts of the corresponding star. Performed with all three stars and considering

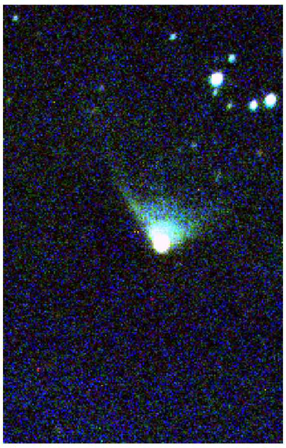

(a) Color image of PV Cep using the images of Fig. 38

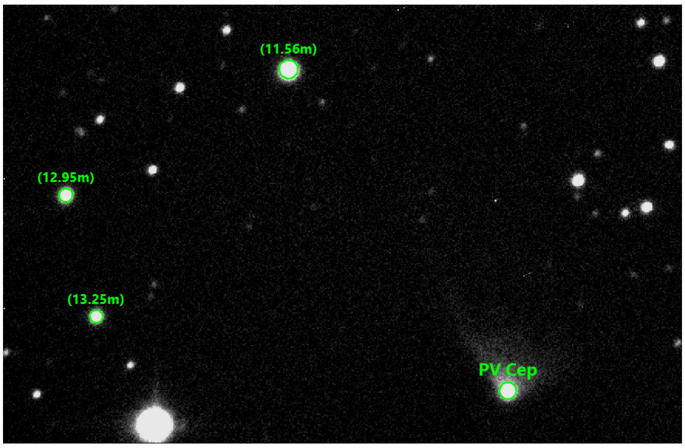

(b) i-Band image of PV Cep and surrounding stars. Bin: 2x2. Stack: 2x240 s, magnitudes of nearby stars in the I-band according to Simbad [8].

Figure 39: Color image and I-band brightness of PV Cep and surrounding stars

errors by using the maximum error method, we get the value of $(12.3 \pm 0.6) mag$ for PV Cep. There are discrepancies regarding the used filter, as Simbad gives the value for the I band from the Johnson UBVRI photometric system and we used the Sloan i-filter. Nonetheless, this value is significantly different from the value of 14.6 mag given by Simbad, which is based on a measurement by [24]Kun et al. 2009.

Star	I brightness	Photon count sum of the star
2MASS J20461128+6800012	11.56	$(3.29 \pm 0.05) \cdot 10^6$
2MASS J20462889+6759054	12.95	$(0.94 \pm 0.05) \cdot 10^6$
2MASS J20462650+6758118	13.25	$(0.76 \pm 0.05) \cdot 10^6$
PV Cep	14.60	$(1.8 \pm 0.5) \cdot 10^6$

Table 8: I-Brigthness and determined i count sum for PV Cep and surrounding stars (using the program ds9).

6.14 V1982 Cyg

Object observed: 21 May 2016

V1982 Cyg is the illuminating star of the reflection nebula Gyulbudaghian 98-171 in the constellation Cygnus.
The object was observed with the V, r and i filters.

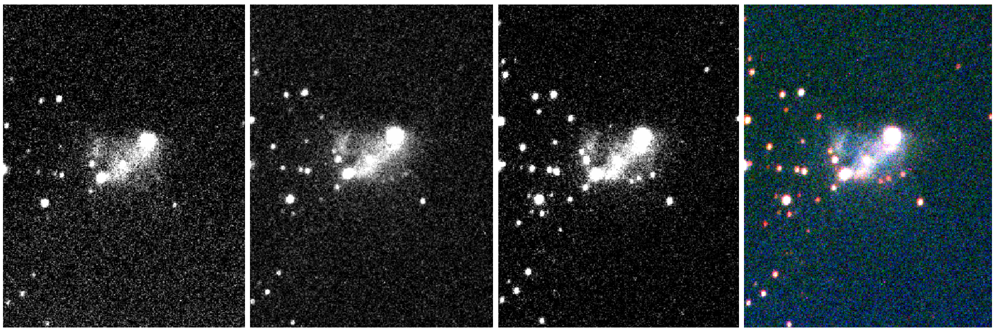

(a) V1982 Cyg in V-Band. Exp.time: 240 s, scale: lin, 7200-10500, maxt: 65000, bckgr: 7500 ± 50

(b) V1982 Cyg in r-Band. Exp.time: 240 s, scale: lin, 6638-11000, max: 65000, bckgr: 7050 ± 30

(c) V1982 Cyg in i-Band. Exp.time: 240 s, scale: lin, 3000-6000, max: 65000, bckgr: 3260 ± 10

(d) Color composite of V1982 Cyg

Figure 40: V1982 Cyg in different filters. Bin: 3x3

As is shown in Figs. 40a - 40c, the nebula is visible in all three filters. The star V1982 Cyg is sitting on the northeast end of the nebula. There are several stars that are in front of the nebula or shine trough it. Some interesting features could be observed: as the color image of V1982 Cyg shows (Fig.40d, where red is infrared), it appears that the structures seen in the infrared are more concentrated in small patches along the southeast direction from the star, while in the red and in the visual the nebulosity is more evenly distributed. Notably, there are a lot more stars seen in i, probably due to extinction. There are almost no stars seen in the west, north and south of the nebula. That's because the nebula lies in the galactic plane and right on the edge of a giant dark molecular cloud of the milky way.

6.15 GM 1-27

Object observed: 21 May 2016

GM 1-27 (or GN 20.18.3) is a reflection nebula in the constellation Cygnus. The object was observed with the filters r and i.

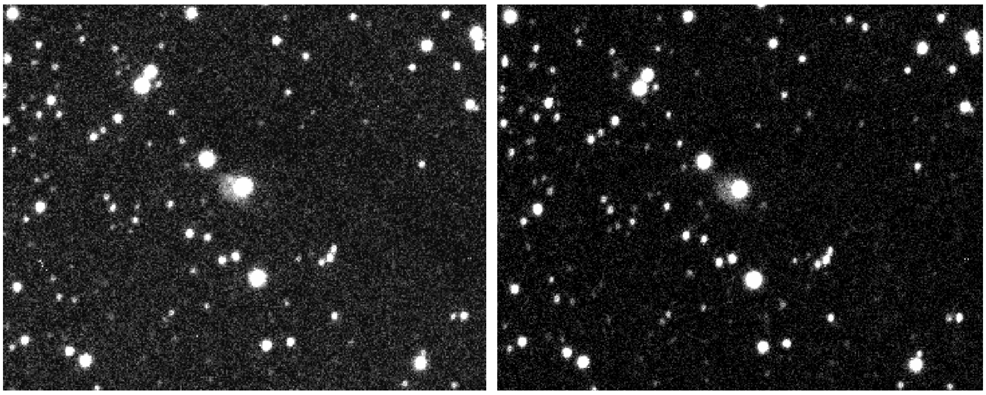

(a) GM 1-27 in r-Band. Exp.time: 200 s, scale: lin, 6200-17400, max: 65000, bckgr: 6270±30

(b) GM 1-27 in i-Band. Exp.time: 200 s, scale: lin, 3080-10300, max: 65000, bckgr: 3130±20

Figure 41: GM 1-27 in the filters r and i. Binning: 3x3

Fig. 41 shows the observed reflection nebula. GM 1-27 is clearly visible as compact nebulosity surrounding the star in the center of the image. This star is not the illuminating star of the nebula, which is in fact a very faint star (I = 17) on the western apex of the nebula ([25]Magakian and Movsessian 1995). The nebula does appear as a compact patch between the star in the center of the image and the star northeast to it, but it is a cometary shaped nebula which extends to the west. This could be suspected on the r-band image. An interesting note: the dark cloud that the nebula is believed to be a part of is visible, especially in the r-band (due to extinction). It begins to the north of the nebula and extends to the southwest. The inner, dense part of the cloud is significantly below the background countrate.

6.16 RNO 129

Object observed: 21 May 2016

RNO 129 is a young object in the constellation Cepheus. It is a star formation region, its distance is 300 pc and it contains several Herbig Haro objects ([26]Movsessian and Magakian 2004).
The object was observed with the filters r and i.

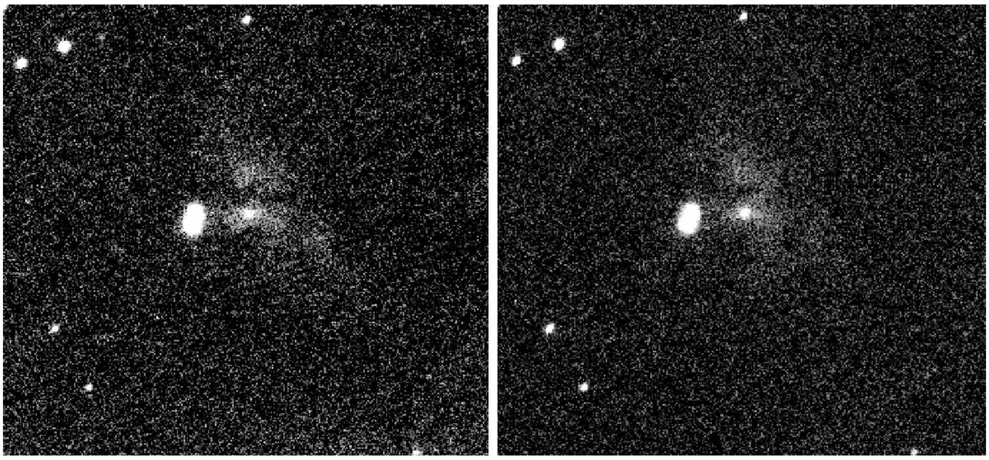

(a) RNO 129 in r-Band. Stack: (180 + 360)s, scale: log, 25800-30000, max: 50000, bckgr: 26000 ± 50

(b) RNO 129 in i-Band. Exp.time: 180 s, scale: log, 3600-4680, max: 12000, bckgr: 3760 ± 20

Figure 42: RNO 129 in the filters r and i. Bin: 3x3

The dominant object is a star lying at the western tip of the nebulosity. It is surrounded by a sharp and bright reflection nebula extending to the north of it, which looks like an elongated nebulosity on the images. Just to the east of this star is another nebulosity patch, beeing illuminated by the star right at its center. To the north of it is another part of the nebula and to the east there is the Herbig Haro object HH 198, just marginally visible.

6.17 V375 Lac

Object observed: 21 May 2016

V375 Lac is a Herbig Ae/Be star in the constellation Lacerta. Its bipolar reflection nebula (which has the shape of an "X") was searched for.
The object was observed with the filters r and i.

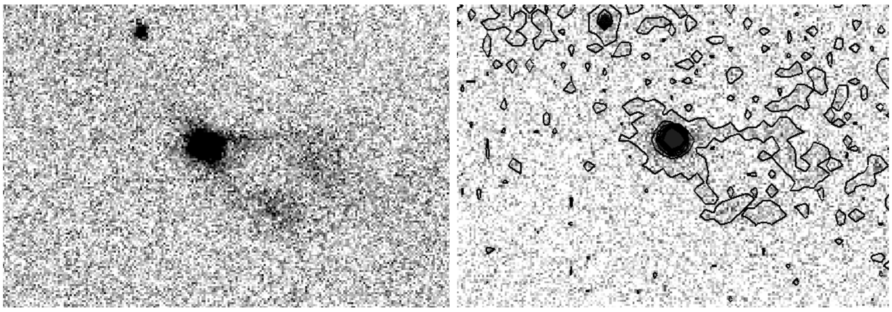

(a) V375 Lac in r-Band. Exp.time: 240 s, scale: lin, 22100-23250, max: 65000, bckgr: 22340 ± 50

(b) V375 Lac in i-Band. Exp.time: 240 s, scale: lin, 30200-31700, max: 65000, bckgr: 30350 ± 70

Figure 43: V375 Lac in the filters r and i. Bin: 3x3

The color map of both images in Fig.43 is inverted for a better visibility of the faint nebulosity. In r, the west part of the bipolar nebula, shaping a ring, is visible as well as the faint extension to the northeast. In i, a contour plot is used to enhance the structure. The east part of the nebula is not visible in both images, although the area is in r significantly above the background. Under the given conditions and with the used exposure time, the overall structure of this nebula is just on the edge of being observable. The east part of the bipolar structure was not resolvable.

6.18 Proto-PN: Red Rectangle

Object observed: 20 April 2016

The Red Rectangle is a protoplanetary nebula with a distinct rectangular shape in the constellation Monoceros. The central star of this bipolar nebula is a post - AGB star (HD 44179).
The object was observed with the filters V, r and i.

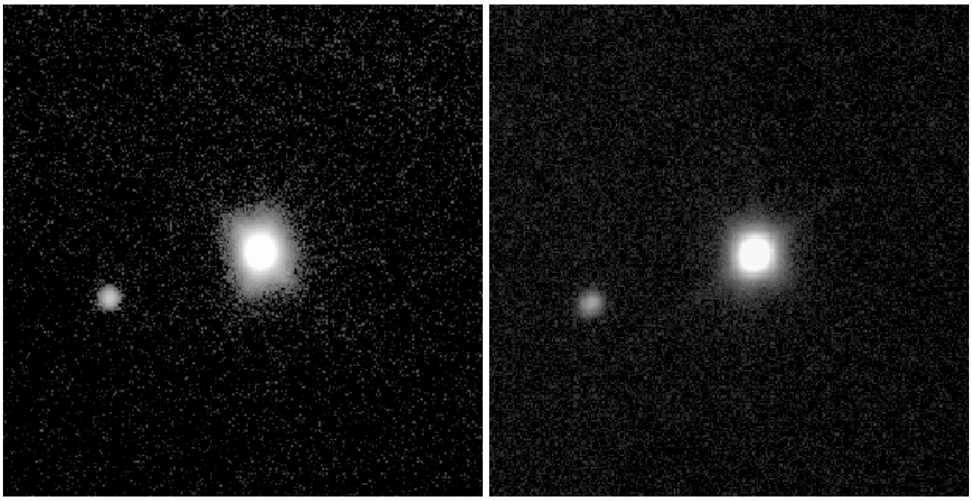

(a) Red Rectangle in r-Band. Stack: (120 + 300)s, scale: log, 47300-83300, max: 200000, bckgr: 46900 ± 100

(b) Red Rectangle in i-Band. Exp.time: 240 s, scale: log, 8280-29930, max: 65000, bckgr: 8500 ± 50

Figure 44: Red Rectangle in the filters r and i. Bin: 2x2

Fig. 44a shows the object in the r-band. The rectangular shape of the nebula is clearly visible. The X-shape along the diagonals of the rectangle is visible as well. The central star is very luminous. A careful scaling and adjusting of the contrast is required to reveal the structure. In Fig. 44b the rectangular shape is not visible in the i-band. The shape was also not visible in the V band at 1x1 binning, which is the reason why this image is not included here.

6.19 Proto-PN: Frosty Leo

Object observed: 17 March 2016, 14 April 2016

The Frosty Leo Nebula is a protoplanetary nebula in the constellation Leo. Just like the Red Rectangle, the origin of this bipolar nebula is a post-AGB star.
The object was observed with the filters B, V, r and i.

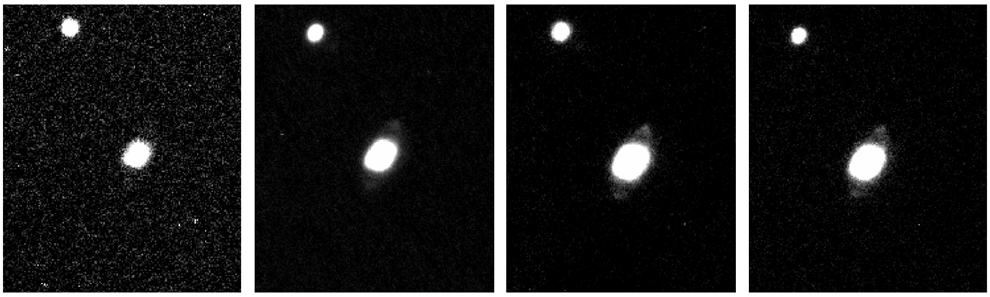

(a) Frosty Leo in B-Band. Stack: (120 + 300)s, scale: lin, 44500-108500, max: 150000, bckgr: 47700 ± 200

(b) Frosty Leo in V-Band. Stack: (2x120 + 2x300)s, scale: lin, 56800-140550, max: 250000, bckgr: 57000 ± 100

(c) Frosty Leo in r-Band. Stack: (120 + 300)s, scale: lin, 31200-68600, max: 130000, bckgr: 31500 ± 100

(d) Frosty Leo in i-Band. Exp.time: 120 s, scale: lin, 5160-18760, max: 65000, bckgr: 5440 ± 30

Figure 45: Frosty Leo in different filters. Bin: 2x2

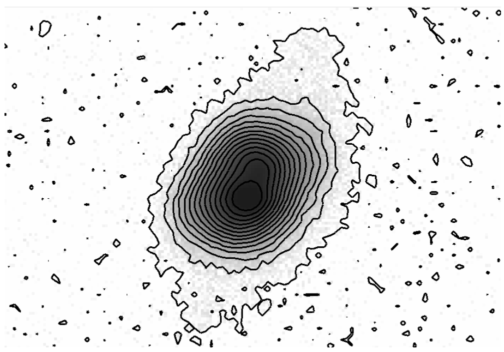

Figure 46: Frosty Leo in V-Band. Stack: (120 + 3x180)s, Bin: 1x1, contour plot and inverted color map.

Fig. 45 shows the observations of Frosty Leo in different filters. Here, the contrast was adjusted to reveal the outer part of the nebula. Except for B, the bipolar structure along the northwest-southeast direction is visible, looking somewhat like a ring around the inner, brighter part. The bright inner part also appears clearly not stellar. Fig. 46 shows a contour plot to reveal the inner bipolar structure of the nebula. For this

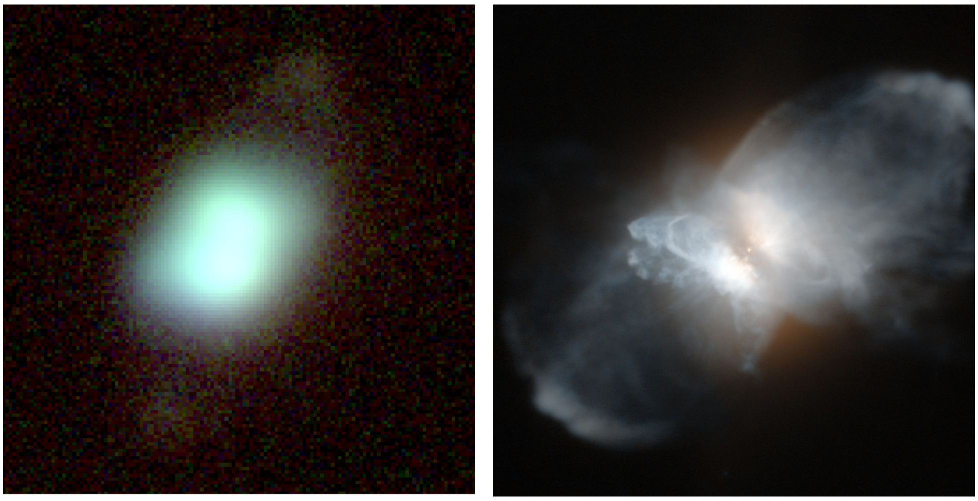

(a) Color image of Frosty Leo, ranging from infrared to visual

(b) Frosty Leo from the Hubble Space Telescope. Credit: ESA/Hubble & NASA

Figure 47: Frosty Leo color images from OLG and HST.

image, a 1x1 binning was used to enhance the resolution.
A color image was made and is shown in Fig. 47a, with i as red, r as green and V as blue. A Hubble Space Telescope image is given for comparison. The scale of both images is roughly the same. The two bright areas visible at the center of the nebula on the HST image appear as the bipolar center of our OLG image. Due to seeing, the division between the bright areas (where the illuminating star lies) was not clearly resolvable. The HST image is slightly tilted to the west.

7 Discussion

As the observations were primarily depending on the weather conditions, the possible observation dates were quite restricted. All 4 clear nights that were used for observations were not favourable regarding the position of the moon, resulting in a bright night sky. Additionally, the observation time in spring is an unfavourable time to observe young stellar objects, because there are only a few YSOs visible in the sky. Since the pre-main sequence phase is a very short phase in the lifetime of a star, almost all observable YSOs are located within some degree of the galactic plane (where nearly all star forming regions of our galaxy are). In a typical spring night in April on the northern hemissphere at 47° latitude, the galactic plane lies beneath Polaris in the northern celestial part with a maximum altitude of 20° - 30° above the horizon. This is a very suboptimal condition for observations, the negative effects of the seeing at low altitudes have already been discussed. Additionally, by passing through more volume of the earth's atmosphere, the starlight gets strongly influenced by it, especially affecting shorter wavelengths by scattering. Two approaches were used to reduce these negative effects. First, using the first half of the night in the early part of spring, where the galactic plane is visible in the 'winter' constellations (Monoceros, Orion, Gemini, Taurus, Auriga and Perseus). The observations had to be done quickly, as the objects approached the western horizon. The central part of the city of Graz also lies to the west of the OLG, which led to an even brighter sky due to light pollution. The second idea was to use the second half of the night later in spring to observe the YSOs of the then rising 'summer' constellations (Cygnus, Lacerta, Cepheus, Cassiopeia). The problem then was (beside the moon) the early rising time of the sun, making the observation again a race against time. The perfect observation time for YSOs would be winter or summer. Here, bad weather prevented the observation of YSOs in winter. Inaccuracies in the tracking of the telescope at certain points at long exposure times caused further problems. The conditions were far from perfect for the observations, thus we now look at the results under the given conditions.

The images in the B-band mostly showed the fewest structures in the observations, although many of the observed nebulae should appear blue. There are several possible causes:

- The quantum efficiency of the camera is lower at shorter wavelengths
- The bandwidth and transmittance of B is small (comparing to r and i)
- The bright night sky caused by the moon. Short wavelengths get scattered more by the earth's atmosphere than longer wavelengths, hence the blue sky at daytime. The same effect is seen at night with the reflected sunlight from the moon. The high blue background would make it more difficult to detect faint blue nebulae.
- The previously mentioned scattering of the blue starlight itself by the atmosphere at low altitude.

The best results were made in the V-, r- and i-band. The camera has the best QE in V and r, and the Sloan passbands r as well as i have a broad bandwidth. Also, these longer wavelength are less affected by the bright nightsky. That's the reason for mainly using these filters for observations.

Different binning modes were tested. The 9x9 binning was of no use since the spatial resolution got too bad. For detecting and "snap shooting" the nebulae, the 3x3 binning appeared to be ideal. The resolution is acceptable ($0.75''/pix$), while the exposure times don't have to be very long to get a good SNR. Also, the determined seeing disks were 5-20 times bigger than the angular resolution (which is with $0.277''$ about 1 pixel on a 1x1 binned image at $0.251''/pix$), so we don't lose that much more information at a 3x3 binning. The seeing strongly disturbes 1x1 and 2x2 images. Under these conditions, a 3x3 binning would be sufficient for all observations, according to the seeing determination. The 2x2 binning was used to make more detailed observations of one object in particular. It was utilized when the object already was very clearly visible (e.g. NGC 2261) and a better resolution of particular structures was required. But this binning needed more time, and time was a problematic factor. The 1x1 binning was not very often used, because it needed very long exposure times to reach a similar SNR as the 3x3 binning. It was used for the protoplanetary nebulae (to detect the inner bipolar nature of Frosty Leo or further structures in Red Rectangle). Under optimal conditions, the seeing disks would still cover at least 2 or 3 pixels, making the 1x1 binning unfavourable to gain a better resolved image of the observed objects. In the end, the 3x3 binning would be the ideal choice. Nonetheless, the stacking gets much more accurate when performing on an image with higher resolution (more pixels available) while stacking with 3x3 binning requires exact pixel-by-pixel accuracy which was not always possible.

There were only few nebulae that were not detected during the observations. Holoea was just on the edge (being a really faint infrared object), HK Ori was just detectable by a small count number difference (appears blue and was close to the horizon). RY Tau and XY Per were not significantly detected. The cause for this could be the low altitude, as both RY Tau and XY Per (observed on 20 April 2016, two days before full moon) had an altitude of $< 15°$ on the western horizon above the city of Graz (5 min exposure time in r with 3x3 binning saturated the whole detector). All other objects that were observed were clearly detected.
The first thing noticable was that bright, compact nebulosities nearby the illuminating star got observable pretty easy, while detecting outer, dimmer parts of the nebula was quite difficult. Often the inner part got well beyond saturation before even some outer features were visible (examples: AB Aur, FU Ori and V628 Cas). It was quite usual that the illuminating star got saturated while trying to get the nebula visible. To avoid this, one would have to make exposure times short but using a lot of images of the same objects and stack them together. A process that would take too much time for every single nebula.
Few nebulae showed bright features even at short exposure times, with NGC 2261 (Hubble's Variable Nebula) being the most favourable object. It is also the object

that appears most extended on the sky. Most of the YSOs have known Herbig Haro objects surrounding them. These are usually small visual nebulosity patches, but often too small to detect them with the telescope at the OLG. An exception being the observed HH located to the east of RNO 129.

As every object that is discussed in this work could fill (and in 90% of the cases already has filled) whole papers dedicated to them or even to small features of them, a lot of possible analyses were not made (e.g. photometry of all objects, calculating every physical expansion). This would exceed the goal and work of this bachelor thesis. A set of different analysis for different objects were made to focus on individual interesting properties and also as a learning practice. The main object was the observations and the editing of the images to achieve the best result possible with the existing devices and conditions.

8 Summary

A number of different reflection nebulae were observed at the OLG, focusing primarily on YSOs. Images were taken with different bands and were processed by data reduction and stacking to improve the quality. From these images, physical properties of the objects as well as seeing conditions were determined. The optimal conditions and camera settings to observe reflection nebulae were discussed, considering seeing conditions, possible angular resolution and binning as well as celestial positions of the objects. The observed objects are listed in chapter 4. Images, information and analysis on the objects are in chapter 6.

9 Acknowledgement

The information on the theory of stellar evolution is primarily based on lecture notes from 'Stellar Structure & Stellar Evolution' from lecturer Dr. Thorsten Ratzka at the Karl-Franzens Universität Graz.

Thanks to Reiner Vogel for providing a catalogue of young stellar objects with observation notes, which was a basis for choosing the different YSOs.

References

[1] J. S. Mathis, W. Rumpl, K. H. Nordsieck. *The size distribution of interstellar grains.* apj **217** (1977) 425.
doi:10.1086/155591

[2] R. D. Schwartz. *Herbig-Haro objects.* Annual review of astronomy and astrophysics **21** (1983) 209.

[3] I. Iben Jr, A. Renzini. *Asymptotic giant branch evolution and beyond.* Annual Review of Astronomy and Astrophysics **21** (1983) 271.

[4] K. M. Volk, S. Kwok. *Evolution of protoplanetary nebulae.* The Astrophysical Journal **342** (1989) 345.

[5] SBIG. STF-8300M Typical specifications. https://www.sbig.com/products/cameras/stf-series/stf/stf-8300m/. Accessed: 3 Jul 2016.

[6] M. S. Bessell. *Standard photometric systems.* Annu. Rev. Astron. Astrophys. **43** (2005) 293.

[7] SBIG. Photometric systems. https://www.sbig.com/science-education/science_education/about-photometry/. Accessed: 24 Jul 2016.

[8] M. Wenger, F. Ochsenbein, D. Egret, P. Dubois, F. Bonnarel, S. Borde, F. Genova, G. Jasniewicz, S. Laloë, S. Lesteven, R. Monier. *The SIMBAD astronomical database. The CDS reference database for astronomical objects.* aaps **143** (2000) 9.
doi:10.1051/aas:2000332

[9] Österreichischen Akademie der Wissenschaften. Observatorium Lustbühel Graz. http://www.austriaca.at/sternwarten/lustbuehel.htm, 2005. Accessed: 24 Jul 2016.

[10] R. Köhler, M. Kasper, T. Herbst, T. Ratzka, G.-M. Bertrang. *Orbits in the T Tauri triple system observed with SPHERE.* Astronomy & Astrophysics **587** (2016) A35.

[11] L. Loinard, R. M. Torres, A. J. Mioduszewski, L. F. Rodríguez, R. A. González-Lópezlira, R. Lachaume, V. Vázquez, E. González. *VLBA determination of the distance to nearby star-forming regions. I. The distance to T Tauri with 0.4% accuracy.* The Astrophysical Journal **671** (2007) 546.

[12] O. Morata, Y.-J. Kuan, P. T. P. Ho, H.-C. Huang, E. A. Magnier, R. Zhao-Geisler. *Millimetric and Submillimetric Observations of IRAS 05327+3404 "Holoea" in M36.* aj **146** (2013) 49.
doi:10.1088/0004-6256/146/3/49

[13] Stsc. Digitized Sky Survey. http://alasky.u-strasbg.fr/DSS/DSSColor/. Accessed: 22 Jul 2016.

[14] G. H. Herbig. *Eruptive phenomena in early stellar evolution.* apj **217** (1977) 693.
doi:10.1086/155615

[15] L. Hartmann, S. J. Kenyon. *On the nature of FU Orionis objects.* apj **299** (1985) 462.
doi:10.1086/163713

[16] E. P. Hubble. *The variable nebula NGC 2261.* apj **44** (1916).
doi:10.1086/142284

[17] H. M. Johnson. *Hubble's variable nebula NGC 2261.* aj **71** (1966) 224.
doi:10.1086/109910

[18] B. F. Jones, G. H. Herbig. *Proper motions of Herbig-Haro objects. II - The relationship of HH-39 to R Monocerotis and NGC 2261.* aj **87** (1982) 1223.
doi:10.1086/113205

[19] L. M. Close, F. Roddier, J. Hora, J. Graves, M. Northcott, C. Roddier, W. Hoffman, A. Dayal, G. Fazio, L. Deutsch. *Adaptive optics infrared imaging polarimetry and optical hst imaging of hubble's variable nebula (r monocerotis/ngc 2261): a close look at a very young active herbig ae/be star.* The Astrophysical Journal **489** (1997) 210.

[20] L. Asselin, F. Ménard, P. Bastien, J.-L. Monin, D. Rouan. *The Environment of V633 Cassiopeiae and V376 Cassiopeiae: Evidence for Circumstellar Disks.* The Astrophysical Journal **472** (1996) 349.

[21] Á. Kóspál, P. Ábrahám, D. Apai, D. Ardila, C. Grady, T. Henning, A. Juhász, D. Miller, A. Moór. *High-resolution polarimetry of Parsamian 21: revealing the structure of an edge-on FU Ori disc.* Monthly Notices of the Royal Astronomical Society **383** (2008) 1015.

[22] H. G. Arce, A. A. Goodman. *The Great PV Cephei Outflow: A Case Study in Outflow-Cloud Interaction.* The Astrophysical Journal **575** (2002) 911.

[23] V. Straizys, K. Cernis, A. Kazlauskas, E. Meistas. *On the distance of dark clouds in the vicinity of the reflection nebula NGC 7023 in Cepheus.* Baltic Astronomy **1** (1992) 149.

[24] M. Kun, Z. Balog, S. J. Kenyon, E. E. Mamajek, R. A. Gutermuth. *Pre-Main-Sequence Stars in the Cepheus Flare Region.* The Astrophysical Journal Supplement Series **185** (2009) 451.

[25] T. Y. Magakian, T. Movsessian. *GM1-27: A cometary nebula associated with anisotropic outflow.* Astronomy and Astrophysics **295** (1995) 504.

[26] T. A. Movsessian, T. Y. Magakian. *A study of the star-forming group RNO 129.* Astronomy Reports **48** (2004) 988.
doi:10.1134/1.1836022